

FINAL STAGES OF MASSIVE STARS. SN EXPLOSION AND EXPLOSIVE NUCLEOSYNTHESIS

M. Limongi¹ and A. Chieffi¹

Abstract. We review the presupernova evolution, the explosion and the explosive nucleosynthesis of massive stars in the range 11–120 M_{\odot} . We mainly focus on the advanced evolutionary phases prior to the explosion, *i.e.* from the core He exhaustion up to the onset of the iron core collapse.

1 Introduction

Massive stars, exploding as core collapse supernovae, play a pivotal role in the global evolution of the Universe.

The first massive stars (the so-called PopIII stars), *i.e.*, those formed out of metal-free gas at redshift $z \sim 10$, contributed significantly to the reionization of the matter at the end of the dark age because of their very high surface temperature (Tumlinson & Shull 2000; Bromm *et al.* 2001). Moreover, because of their relatively short evolutionary lifetimes they were also responsible for a prompt initial enrichment of the intergalactic medium with heavy elements (Mori *et al.* 2002; Bromm *et al.* 2003; Wada & Venkatesan 2003; Yoshida *et al.* 2004).

Massive stars also significantly contribute to the chemical and dynamical evolution of the galaxies. In fact, they (1) provide most of the mechanical energy input into the interstellar medium through strong stellar winds and supernova explosions (Abbott 1982) and hence induce star formation and mixing of the interstellar matter; (2) generate most of the ultraviolet ionizing radiation and power the far-infrared luminosities of galaxies through the heating of the dust; (3) contribute significantly to the integrated luminosity of the unresolved galaxies (since they are very luminous objects); (4) synthesize most of the elements (with $4 < Z < 38$), especially those necessary to life; (5) produce some long-lived radioactive nuclei like, *e.g.*, ^{26}Al , ^{60}Fe and ^{44}Ti that give important information on

¹ INAF Osservatorio Astronomico di Roma, via Frascati 33, 00040 Monteporzio Catone Roma, Italy; e-mail: marco@oa-roma.inaf.it;
e-mail: alessandro.chieffi@iasf-roma.inaf.it

the ongoing nucleosynthesis in the Galaxy - these gamma ray emitters constitute the main observational targets of the gamma ray satellites presently in space (*i.e.*, INTEGRAL, RHESSI) (Limongi & Chieffi 2006); (6) constitute the most energetic phenomenon yet found, emitting gamma-ray bursts as they collapse into black holes (Woosley 1993; Bloom *et al.* 2002; Price *et al.* 2002). Moreover, the interiors of massive stars constitute invaluable laboratories with physical conditions not seen elsewhere in the universe. For example, the neutrino burst occurring few seconds prior their explosion is one of the most powerful events in the universe. Then, the understanding of the evolution and the explosion of massive stars is of paramount importance in astrophysics.

We review here the presupernova evolution, the explosion and mostly the nucleosynthesis of massive stars. We mainly focus on the advanced evolutionary phases prior to the explosion, *i.e.* from the core He exhaustion up to the onset of the iron core collapse, and leave to others all aspects of massive stellar evolution during H- and He-burning (see the excellent reviews by Maeder & Conti 1994; Massey 2003; and Meynet this book). However, since the advanced burning phases strongly depend on the evolutionary history of the star during the H- and He-burning stages, here we address only the aspects of these phases relevant for the further evolution of the star up to the explosion. In particular we discuss in some detail the effect of mass loss during H- and He-burning and its implications on the more advanced burning phases. We also very briefly outline the current understanding of the mechanism of core collapse supernova explosion. The explosive nucleosynthesis as well as the contribution of massive stars to the global enrichment of the interstellar medium and their role in the chemical evolution of the galaxies is, on the contrary, described in detail.

2 Massive Stars: General Overview

Stars are self-gravitating objects of hot plasma, emitting energy in the form of photons from the surface and/or neutrinos from the center, in hydrostatic equilibrium. The equilibrium is guaranteed by the balance between the pressure gradient – the pressure being provided by a combination of radiation, ideal gas and partially or totally degenerate electrons - and the force of gravity:

$$\frac{dP}{dr} = -\frac{GM(r)\rho(r)}{r^2} \quad (2.1)$$

where $M(r)$ is the mass interior to radius r and $\rho(r)$ is the corresponding density.

Since the star must radiate (because it is hotter than the environment), for the virial theorem it heats up and shrinks at the same time. If the equation of state is of the form $P = (\gamma - 1)\rho e$, the variation of both the internal and the gravitational energy are related to the luminosity by:

$$L = -\dot{E}_{grav} \frac{(3\gamma - 4)}{3(\gamma - 1)} = -\dot{E}_{int}(4 - 3\gamma).$$

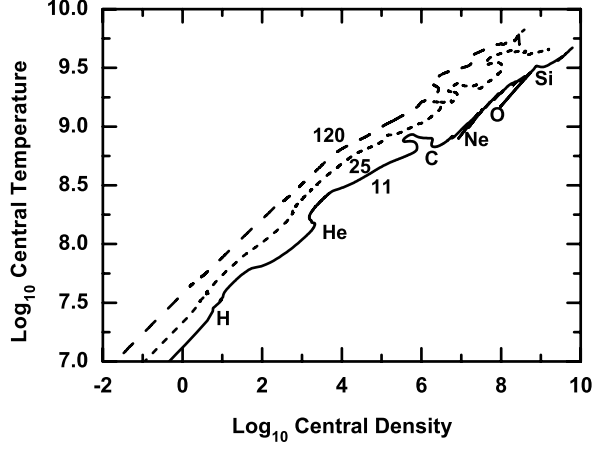


Fig. 1. Path followed by the center of the computed models in the Temperature-Density diagram; the main nuclear burning stages are shown in the figure.

If $\gamma > 4/3$ the star replaces the energy radiated away by a slow secular contraction. In this case a fraction of the gravitational energy gained by the contraction goes into internal energy and hence the star heats up. When the central temperature is high enough the nuclear reactions take place, the nuclear energy supplies the energy lost as radiation and/or neutrinos, and the gravitational contraction halts. As the nuclear fuel is exhausted, gravitational contraction and heating start again until the next nuclear fuel is ignited. From this point of view the life of a star can be envisioned as the progressive gravitational contraction of a self-gravitating ball of gas punctuated by occasional delays when the nuclear burning supplies the energy lost as radiation or neutrinos. Low-mass stars ($M \leq 8 M_{\odot}$) reach a point where the internal structure is fully supported by the electron degeneracy and the contraction of the degenerate core is slowed down. Moreover, mass loss prevents the degenerate core to reach the Chandrasekhar mass and the star to explode as supernova. Hence these stars end their evolution as white dwarfs. More massive stars, on the contrary, never experience a significant electron degeneracy in the core during all their nuclear burning stages hence they evolve to higher and higher temperatures, fusing heavier and heavier elements until a iron core is formed.

The run of the central temperature as a function of the central density for a star of a given mass can be simply estimated by replacing Equation (2.1) with average values between center and surface, by adopting an equation of state for an ideal gas and by assuming a constant density model:

$$T_c \propto \rho_c^{1/3} M^2. \quad (2.2)$$

Figure 1 shows the path followed by evolutionary models of massive stars (*i.e.* computed without any kind of approximation) in the $\text{Log}T_c - \text{Log}\rho_c$ plane. For each models, the central temperature roughly scales as $\rho_c^{1/3}$ during all the evolution

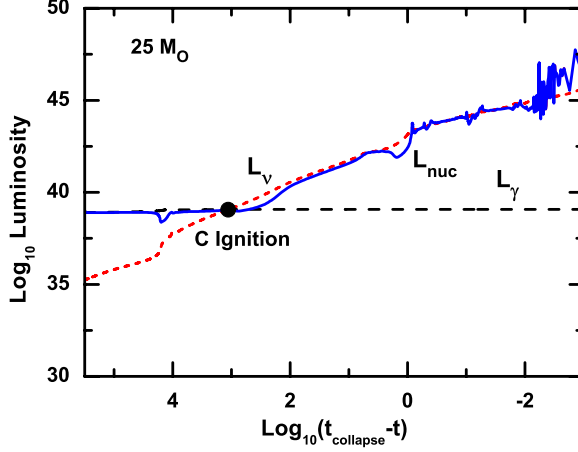


Fig. 2. Temporal behavior of the various luminosities for a $25 M_{\odot}$ model: photons (*black dashed line*), neutrinos (*red dotted line*) and nuclear (*blue solid line*). Core C ignition is marked by the big filled black dot.

and hence the basic relation 2.2 is a good approximation of the central behavior of massive star.

2.1 Neutrino Losses

Neutrino losses are an important aspect of the evolution of a massive star. In fact, in very hot environments there are enough photons in the Planck distribution having energies in excess of $m_e c^2$, where m_e is the electron rest mass. As a consequence the creation of positron-electron pairs proceeds at a high rate. The created (e^+e^-) pairs quickly recombine and give back two photons per pair. Since the lifetime of pair annihilation is very short the pair creation and annihilation quickly come to an equilibrium. However, in this continuous back and forth exchange there is a small one-way leakage since a small fraction of (e^+e^-) recombinations result in a pair ($\nu_e, \bar{\nu}_e$) instead of two photons:

$$\gamma + \gamma \rightleftharpoons e^+ + e^- \rightarrow \nu_e + \bar{\nu}_e.$$

Since the neutrinos exit the star at the speed of the light (while positrons, electrons and γ 's remain trapped), this is an efficient energy loss mechanism.

The neutrino emission from pair production starts to become efficient when the central temperature exceeds $\sim 8 \times 10^8$ K and continuously increases all along the further evolutionary phases up to the final collapse. For this reason the advanced evolutionary phases are called “neutrino dominated”. Figure 2 shows the temporal behavior of the surface luminosity (L_{γ} , energy lost by photons), of the neutrino luminosity (L_{ν} , energy lost by neutrinos from the center), and of the nuclear luminosity (L_{nuc} , energy produced by all the nuclear reactions within the star) for

a $25 M_{\odot}$ model. A comparison between the photon and the neutrino luminosities shows that before core C burning the main energy losses occur from the surface of the star through photons while in the more advanced burning stages it occurs mainly from the center through neutrinos. Since the nuclear luminosity is regulated by the energy losses, *i.e.* it refurnishes the star of the energy lost, it closely follows the photon luminosity first and the neutrino luminosity later. When the nuclear reactions are not able to produce enough energy to fully sustain the star the contraction speeds up in order to gain the missing energy from the gravitational field. The dramatic increase of the total luminosity (Fig. 2), combined with the almost constant nuclear energy E_{nuc} provided by each burning stage (see below), implies a dramatic acceleration of the stellar evolution during the advanced burning stages (Table 1). The lifetime of any given nuclear burning stage, in fact, can be simply estimated by the following relation:

$$\tau_{nuc} \simeq E_{nuc} \frac{M}{L}.$$

2.2 Nuclear Networks

The high temperatures typical of the advanced burning stages allow the activation of a great variety of nuclear reactions. In these conditions, in fact, some key reactions releasing light particles (protons, neutrons and α particles) become efficient. The light particles, then, can be captured by almost all the isotopes present in the hot plasma and hence a huge number of nuclear reactions are promptly activated. Such an occurrence has important consequences on the numerical calculations of the advanced nuclear burning phases of massive stars. First of all, it is not possible to follow the evolution of so many nuclear species by adopting analytical formulae or simple approximations. It is necessary, on the contrary, to solve a set of N differential equations describing the chemical evolution of the matter due to nuclear reactions,

$$\begin{aligned} \frac{\partial Y_i}{\partial t} = & \sum_j c_i(j) \lambda_j Y_i + \sum_{j,k} c_i(j,k) \rho N_A \langle \sigma v \rangle_{j,k} Y_j Y_k + \\ & \sum_{j,k,l} c_i(j,k,l) \rho^2 N_A^2 \langle \sigma v \rangle_{j,k,l} Y_j Y_k Y_l \quad i = 1, \dots, s, N, \end{aligned} \quad (2.3)$$

where N is the number of nuclear species included into the nuclear network and the different terms stand for (1) β -decays, electron captures, and photodisintegrations, (2) two-body reactions, and (3) three-body reactions. The coefficients c_i are given by $c_i(j) = \pm N_i$, $c_i(j,k) = \pm N_i / (N_j! N_k!)$, and $c_i(j,k,l) = \pm N_i / (N_j! N_k! N_l!)$, where N_i is an absolute number indicating how many particles i are involved in the reaction, and $N_i!$ prevents double counting for reactions involving identical particles. The sign depends on whether the particle i is produced (+) or destroyed (−). As usual, λ stands for the weak interaction or the photodisintegration rate,

Table 1. Advanced burning stages in massive stars.

Fuel	τ (yr)	T_c (K)	ρ_c (g/cm ³)	L_γ (erg/s)	L_ν (erg/s)
M=11 M_\odot					
H	2.01E+07	3.60E+07	1.04E+01	5.21E+37	5.91E+33
He	1.55E+06	1.80E+08	1.76E+03	1.10E+38	4.60E+34
C	2.02E+04	7.46E+08	4.30E+05	1.91E+38	4.89E+38
Ne	3.56E+03	1.82E+09	5.76E+07	1.99E+38	1.34E+43
O	1.30E-01	1.33E+09	3.10E+07	2.00E+38	1.05E+43
Si	8.34E-01	2.36E+09	2.14E+08	2.00E+38	4.30E+43
M=15 M_\odot					
H	1.25E+07	3.80E+07	7.76E+00	1.31E+38	1.47E+34
He	9.04E+05	1.92E+08	1.19E+03	2.71E+38	1.16E+35
C	1.03E+04	8.15E+08	2.86E+05	4.01E+38	5.00E+39
Ne	2.31E+00	1.58E+09	5.44E+06	4.04E+38	2.90E+42
O	2.42E+00	1.98E+09	9.32E+06	4.04E+38	1.54E+43
Si	3.26E-01	2.98E+09	2.91E+07	4.04E+38	1.04E+45
M=25 M_\odot					
H	6.87E+06	4.08E+07	4.74E+00	4.66E+38	5.65E+34
He	5.27E+05	2.08E+08	7.15E+02	8.68E+38	4.17E+35
C	6.27E+03	8.30E+08	1.73E+05	1.18E+39	8.13E+40
Ne	5.22E-01	1.59E+09	2.45E+06	1.18E+39	2.39E+43
O	6.67E-01	2.10E+09	5.82E+06	1.18E+39	8.87E+43
Si	5.37E-02	3.49E+09	3.72E+07	1.18E+39	2.32E+45
M=35 M_\odot					
H	5.12E+06	4.24E+07	3.73E+00	9.30E+38	1.21E+35
He	4.41E+05	2.15E+08	5.75E+02	1.49E+39	7.45E+35
C	4.01E+03	8.60E+08	1.52E+05	1.53E+39	2.35E+41
Ne	6.33E-01	1.57E+09	2.02E+06	1.57E+39	3.05E+43
O	4.81E-01	2.12E+09	5.19E+06	1.54E+39	1.31E+44
Si	3.94E-02	3.64E+09	3.66E+07	1.52E+39	3.17E+45

while $N_A < \sigma v >$ stands for the two- or three-body nuclear reaction rates. Y_i indicates the abundance by number of the species i ($Y_i = X_i/A_i$, where X_i is the mass fraction and A_i is the atomic weight) (see, *e.g.*, [Fowler *et al.* 1975](#)). A proper treatment of the chemical evolution during the advanced burning stages requires the adoption of very extended nuclear networks, *i.e.*, a large number of nuclear species (N) and nuclear reactions.

Table 1. continued.

Fuel	τ (yr)	T_c (K)	ρ_c (g/cm ³)	L_γ (erg/s)	L_ν (erg/s)
M=60 M_\odot					
H	3.64E+06	4.46E+07	2.73E+00	2.41E+39	3.45E+35
He	3.64E+05	2.23E+08	4.64E+02	2.52E+39	1.52E+36
C	2.54E+03	8.98E+08	1.30E+05	2.61E+39	7.48E+41
Ne	3.20E-01	1.58E+09	1.62E+06	2.73E+39	9.02E+43
O	1.37E-01	2.24E+09	3.30E+06	2.76E+39	8.33E+44
Si	1.12E-02	4.05E+09	5.04E+07	2.74E+39	1.30E+46
M=120 M_\odot					
H	2.76E+06	4.67E+07	2.01E+00	6.28E+39	9.25E+35
He	3.01E+05	2.33E+08	3.48E+02	5.98E+39	3.46E+36
C	1.62E+03	9.71E+08	9.82E+04	6.06E+39	5.62E+42
Ne	1.45E-01	1.55E+09	8.97E+05	6.33E+39	3.39E+44
O	5.03E-02	2.34E+09	2.21E+06	6.38E+39	5.56E+45
Si	1.31E-03	3.65E+09	1.71E+07	6.35E+39	4.57E+46

The structure and evolution of a star in spherical symmetry and hydrostatic equilibrium, without rotation and magnetic fields, is described by a set of four equations, that regulate the physical structure of the star:

$$\frac{\partial P}{\partial M} = -\frac{GM}{4\pi R^4} \quad (2.4)$$

$$\frac{\partial R}{\partial M} = \frac{1}{4\pi R^2 \rho} \quad (2.5)$$

$$\frac{\partial L}{\partial M} = \varepsilon_n + \varepsilon_{grav} + \varepsilon_\nu \quad (2.6)$$

$$\frac{\partial T}{\partial M} = -\frac{GMT}{4\pi R^2 P} \nabla \quad (2.7)$$

(see [Chieffi *et al.* 1998](#) for more details on the meanings of the various terms), supplemented by the system 2.3, describing the chemical evolution. In H- and He-burning these two systems of equations can be solved in two subsequent and separate steps. In fact, in these burning phases the quantities that in principle depend on both the physical and chemical variables (like, *e.g.*, the nuclear energy generation rate ε_n) have a very mild dependence on the chemical composition. Such an occurrence is not valid anymore during the more advanced burning stages. In particular, in these phases ε_n is strongly dependent on both the physical quantities (temperature and density) and the chemical composition and the separate solution of the quoted systems becomes very unstable. A stable solution, on the contrary, requires a full implicit coupling of the two systems and a simultaneous solution of them. Such a full coupling, however, requires also lot of computer time

and memory hence appropriate numerical algorithms and techniques must be developed to solve the problem with the presently available computer machines (see Chieffi *et al.* 1998; Limongi & Chieffi 2003).

2.3 Convection

Probably, the greatest source of uncertainty in the computation of the stellar models is connected to the treatment of convection since we cannot determine, on the basis of first principles, (1) the extension of the convective zones and (2) the velocity of the eddies that is crucial, in the advanced burnings, the convective (τ_{mix}) and nuclear burning (τ_{nuc}) timescales become comparable and a proper treatment of the interaction between convective mixing and local burning is required. An addition problem is also related to the inability of convective mixing to fully homogenize the chemical composition within a single time step. Such an occurrence appears when the mixing timescales become comparable to the typical time steps (Δt).

Convection is commonly treated as a diffusive process and calculated by means of a classical diffusion equation:

$$\frac{dY_i}{dt} = \frac{\partial}{\partial m} \left[(4\pi r^2 \rho)^2 D \frac{\partial Y_i}{\partial m} \right] \quad (2.8)$$

where the diffusion coefficient D is given by $D = 1/3v_cl$, the convective velocity v_c is computed by means of the mixing length theory and l is the mixing length parameter. In principle Equation (2.8) should be added to the pure nuclear terms in Equation (2.3) and a single huge matrix should be solved. Such a coupling would obviously require an enormous computer time and memory. Thus, nuclear burning is usually carried out first and then the convective zones are mixed in a subsequent and separate step (Weaver *et al.* 1978; Nomoto & Hashimoto 1988 and their subsequent works). Note that the models by Limongi & Chieffi (2006) have been computed by fully coupling Equations (2.8) and (2.3).

3 Nuclear Burnings

During its progressive contraction and heating a massive star ignites a successive nuclear burning, either at the center or in a shell, using the products of the previous one as a fuel. Four major (core and/or shell) nuclear burnings, characterized by their principal fuel, can be identified during the evolution from the core He exhaustion up to the presupernova stage, namely, carbon, neon, oxygen and silicon burning. Typically, shell burning occurs at higher temperature and lower density compared to the central burning. In the following we will discuss the basic properties of each burning regardless whether it occurs in the center or in a shell. The detailed nucleosynthesis, on the contrary, can be determined only by solving a nuclear network including as many isotopes and nuclear reactions as possible (depending on the available computer machines).

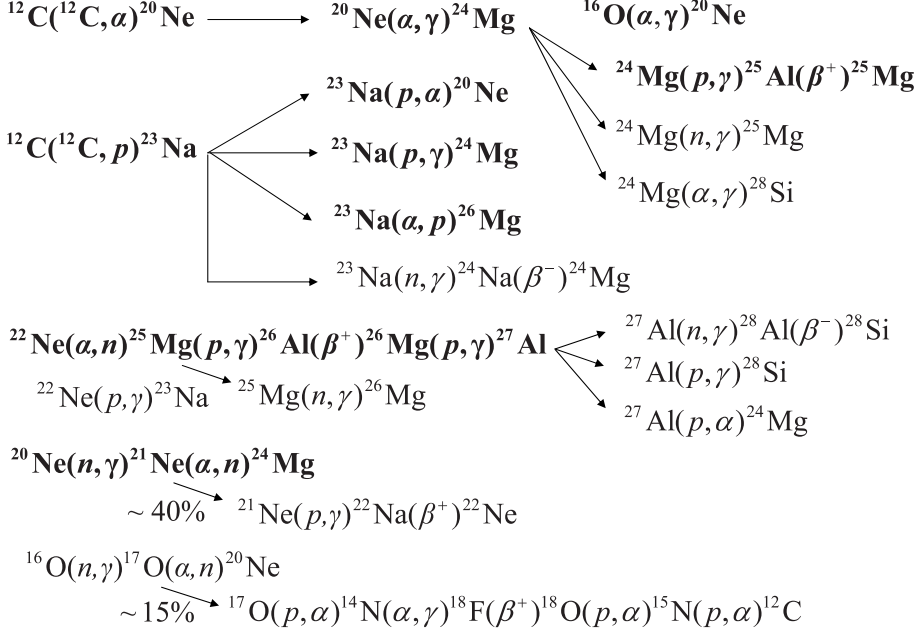


Fig. 3. Important nuclear reactions in carbon burning: the most efficient ones are in bold face.

3.1 Carbon Burning

Carbon burning takes place when the temperature exceeds $T \simeq 7 \times 10^8$ K and is triggered by the two reactions $^{12}\text{C}(^{12}\text{C}, \alpha)^{20}\text{Ne}$ and $^{12}\text{C}(^{12}\text{C}, p)^{23}\text{Na}$ that occur with almost equal branching (Fig. 3). The free protons liberated by the $^{12}\text{C}(^{12}\text{C}, p)^{23}\text{Na}$ are mainly captured by ^{23}Na through the $^{23}\text{Na}(p, \alpha)^{20}\text{Ne}$ and $^{23}\text{Na}(p, \gamma)^{24}\text{Mg}$ reactions. As a consequence ^{23}Na is mainly transformed into ^{20}Ne and ^{24}Mg (Fig. 3). Other efficient sequences involving proton captures are $^{24}\text{Mg}(p, \gamma)^{25}\text{Al}(\beta^+)^{25}\text{Mg}$ followed by $^{25}\text{Mg}(p, \gamma)^{26}\text{Al}(\beta^+)^{26}\text{Mg}$ and $^{26}\text{Mg}(p, \gamma)^{27}\text{Al}$. At the same time most of the α -particles liberated by the $^{12}\text{C}(^{12}\text{C}, \alpha)^{20}\text{Ne}$ are captured by ^{16}O , the most abundant product of He burning, through the $^{16}\text{O}(\alpha, \gamma)^{20}\text{Ne}$, and by ^{20}Ne and ^{23}Na , freshly synthesized, through the reactions $^{20}\text{Ne}(\alpha, \gamma)^{24}\text{Mg}$ and $^{23}\text{Na}(\alpha, p)^{26}\text{Mg}$. This means that the main products of carbon burning are ^{20}Ne , ^{23}Na and ^{24}Mg and a smaller amount of $^{25,26}\text{Mg}$ and ^{27}Al .

It is interesting to note that the reactions discussed so far occur even in stars having zero initial metallicity. This means that all the nuclei produced by these sequences have a primary origin (*i.e.*, no heavy element other than H and He is required for their synthesis). If, on the contrary, some metals are initially present, the efficient reaction $^{22}\text{Ne}(\alpha, n)^{25}\text{Mg}$ is promptly activated and supplements the primary production of ^{25}Mg , ^{26}Mg and ^{27}Al with a secondary component (*i.e.*, a production that scales with the initial metallicity). The ^{22}Ne needed to ignite

such reactions is the result of the conversion of the initial CNO into ^{14}N in H-burning and the following transformation of ^{14}N into ^{22}Ne in He burning through the sequence $^{14}\text{N}(\alpha, \gamma)^{18}\text{F}(\beta^+)^{18}\text{O}(\alpha, \gamma)^{22}\text{Ne}$. Thus the ^{22}Ne mass fraction scales linearly with the initial metallicity (*i.e.*, mainly the initial CNO).

The reactions involving production and destruction of neutrons are particularly important for the *s*-process nucleosynthesis, *i.e.*, the one driven by a sequence of neutron captures slower than the decay times of the unstable nuclei near the stability valley (Burbidge *et al.* 1957). Figure 3 shows that the most efficient neutron source is the $^{22}\text{Ne}(\alpha, n)^{25}\text{Mg}$ that, in turn, scales with the initial metallicity (see above). The most efficient neutron poison is ^{20}Ne via the $^{20}\text{Ne}(n, \gamma)^{21}\text{Ne}$ reaction which is, however, followed by the two reactions $^{21}\text{Ne}(\alpha, n)^{24}\text{Mg}$ and $^{21}\text{Ne}(p, \gamma)^{22}\text{Na}$. Since the first one gives back a neutron, the efficiency of ^{20}Ne as a neutron poison depends on the relative efficiency between the $^{21}\text{Ne}(p, \gamma)^{22}\text{Na}$ and the $^{21}\text{Ne}(\alpha, n)^{24}\text{Mg}$ ($R_{(p,\gamma)/(\alpha,n)} = r_{(p,\gamma)}/r_{(\alpha,n)}$, where r is the reaction rate). Typically $R_{(p,\gamma)/(\alpha,n)}$ decreases with increasing temperature and hence the efficiency of the ^{20}Ne as a neutron poison decreases as well, *i.e.*, it scales inversely with $R_{(p,\gamma)/(\alpha,n)}$. Typical values of $R_{(p,\gamma)/(\alpha,n)}$ as a function of temperature, for a solar metallicity star, are: $R_{(p,\gamma)/(\alpha,n)} \simeq 0.4$, for $T \simeq 8.5 \times 10^8$ K and $R_{(p,\gamma)/(\alpha,n)} < 0.05$ for $T \simeq 1 \times 10^9$ K. This property is valid in general for any neutron capture followed by a series of processes involving the product of the neutron capture in the entrance channel and light particles (including a neutron) in the exit channel. Another example is $^{16}\text{O}(n, \gamma)^{17}\text{O}$ which is followed by $^{17}\text{O}(\alpha, n)^{20}\text{Ne}$ and $^{17}\text{O}(p, \alpha)^{14}\text{N}$ (Fig. 3). Thus, it is difficult to identify, *a priori*, the most efficient neutron poison without a deep analysis of all the reactions involving a capture and a release of neutrons as a function of the temperature and also for any given initial metallicity. Other efficient neutron poisons, with lower rates compared to the $^{20}\text{Ne}(n, \gamma)^{21}\text{Ne}$ are $^{23}\text{Na}(n, \gamma)^{24}\text{Na}$, $^{24}\text{Mg}(n, \gamma)^{25}\text{Mg}$, $^{25}\text{Mg}(n, \gamma)^{26}\text{Mg}$ and $^{27}\text{Al}(n, \gamma)^{28}\text{Al}$ (Fig. 3). The rates of the neutron captures involving the so-called *s*-process elements, *i.e.*, elements heavier than iron, are lower by ~ 2 orders of magnitudes compared to that of the $^{20}\text{Ne}(n, \gamma)^{21}\text{Ne}$ and typically scale inversely with the charge (Z) of the element. In fact, the most efficient neutron captures sequences are $^{57}\text{Fe}(n, \gamma)^{58}\text{Fe}(n, \gamma)^{59}\text{Fe}$, $^{59}\text{Co}(n, \gamma)^{60}\text{Co}$, $^{60}\text{Ni}(n, \gamma)^{61}\text{Ni}(n, \gamma)^{62}\text{Ni}$, $^{56}\text{Fe}(n, \gamma)^{57}\text{Fe}$, $^{62}\text{Ni}(n, \gamma)^{63}\text{Ni}$, $^{63}\text{Cu}(n, \gamma)^{64}\text{Cu}$, $^{65}\text{Cu}(n, \gamma)^{66}\text{Cu}$, $^{66}\text{Zn}(n, \gamma)^{67}\text{Zn}(n, \gamma)^{68}\text{Zn}$ and so on, with progressively decreasing rates. The relative and absolute efficiency of all the reactions discussed so far may vary, even significantly, depending on the mass and metallicity of the star and on whether the burning occurs at the center or in a shell (see, *e.g.*, Limongi *et al.* 2000, Table 3, and also Limongi & Chieffi 2006).

Figure 3 shows the ensemble of reactions most efficient (down to a factor of 1000 of the maximum rate) during carbon burning. These reactions, however, cannot be considered as the minimum set of reactions needed to properly follow the carbon burning. In fact, as we already mentioned above, the light particles (protons, neutrons and α particles) released by the main carbon burning reactions can be captured by almost all the isotopes present in the hot plasma hence an extremely large number of reactions are promptly activated. Thus, the final nucleosynthesis resulting from carbon burning can only be determined by means of a

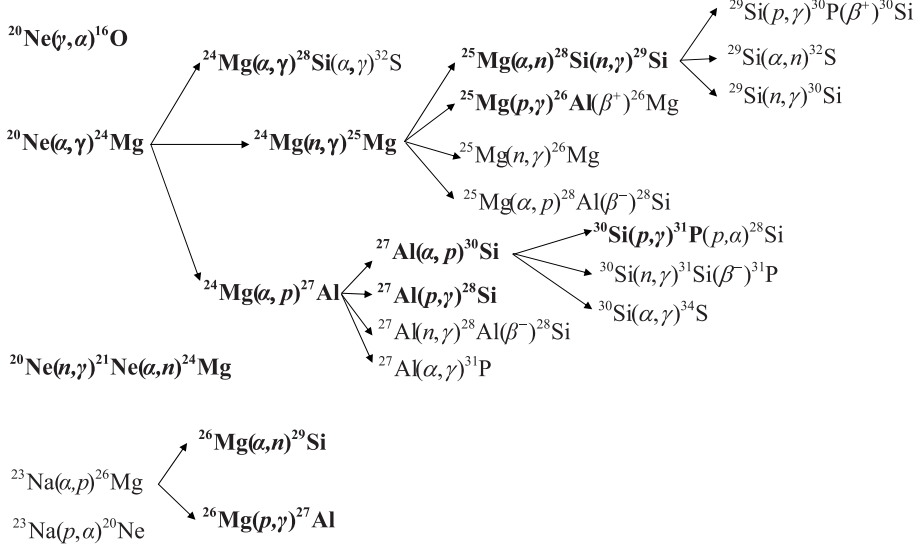


Fig. 4. Important nuclear reactions in neon burning: the most efficient ones are in bold face.

nuclear network including at least some hundreds of isotopes and some thousands of reactions (see Sect. 2.2). This comment is valid in general for all the advanced burnings following He burning (see below).

3.2 Neon Burning

At C exhaustion the chemical composition is dominated by ^{16}O (left over by core He burning and survived to C burning), ^{20}Ne , ^{23}Na and ^{24}Mg . Among these nuclei, ^{16}O is the one having the lowest Coulomb barrier, but before temperatures for oxygen fusion are achieved, the photodisintegration of ^{20}Ne via $^{20}\text{Ne}(\gamma, \alpha)^{16}\text{O}$ is activated. In fact, in general, photodisintegrations start to play a role when $kT \gg Q$ (where Q is the Q-value of the capture reaction). In these conditions a substantial fraction of photons with energies larger than Q exist in the tail of the Plank distribution and the photodisintegration reaction become energetically favored. Since $^{16}\text{O}(\alpha, \gamma)^{20}\text{Ne}$ has a rather small Q-value ($\simeq 4$ MeV), photodisintegration of ^{20}Ne activates at temperatures in excess of $T \simeq 10^9$ K. Most of the free α -particles released by $^{20}\text{Ne}(\gamma, \alpha)^{16}\text{O}$ are captured by the remaining ^{20}Ne leading to ^{24}Mg through the $^{20}\text{Ne}(\alpha, \gamma)^{24}\text{Mg}$ reaction (Fig. 4). Some ^{24}Mg flows to $^{28,29,30}\text{Si}$ mainly through the sequences: $^{24}\text{Mg}(\alpha, \gamma)^{28}\text{Si}$, $^{24}\text{Mg}(n, \gamma)^{25}\text{Mg}(\alpha, n)^{28}\text{Si}$, $^{24}\text{Mg}(\alpha, p)^{27}\text{Al}(\alpha, p)^{30}\text{Si}$, $^{24}\text{Mg}(\alpha, p)^{27}\text{Al}(p, \gamma)^{28}\text{Si}$ (Fig. 4). One of the main products of C burning, ^{23}Na , is completely destroyed via $^{23}\text{Na}(\alpha, p)^{26}\text{Mg}$ and $^{23}\text{Na}(p, \alpha)^{20}\text{Ne}$. Some ^{26}Mg flows to ^{29}Si and ^{27}Al via the (α, n) and (α, p) reactions (Fig. 4).

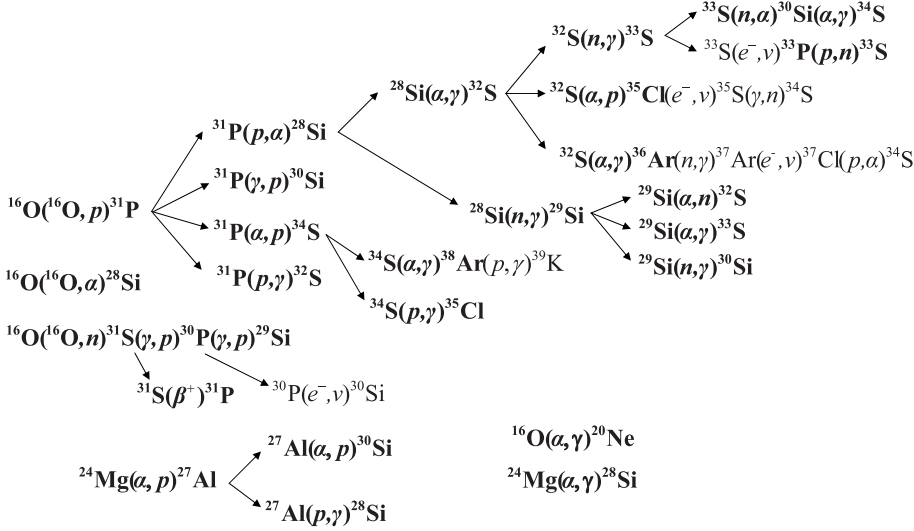


Fig. 5. Important nuclear reactions in oxygen burning: the most efficient ones are in bold face.

Other less efficient reactions of interest to nucleosynthesis (but not to the energy generation) are $^{28}\text{Si}(\alpha, \gamma)^{32}\text{S}$, and the p-, α - and n-captures on $^{29,30}\text{Si}$ leading to the synthesis of ^{31}P and ^{32}S (shown in Fig. 4). In Ne burning, neutrons are mainly produced by $^{26}\text{Mg}(\alpha, n)^{29}\text{Si}$, $^{25}\text{Mg}(\alpha, n)^{28}\text{Si}$ and $^{29}\text{Si}(\alpha, n)^{32}\text{S}$ while they are mainly absorbed by $^{24}\text{Mg}(n, \gamma)^{25}\text{Mg}$, $^{28}\text{Si}(n, \gamma)^{29}\text{Si}$, $^{27}\text{Al}(n, \gamma)^{28}\text{Al}$ and $^{29}\text{Si}(n, \gamma)^{30}\text{Si}$. The final composition after Ne burning is enhanced in ^{16}O , $^{24,25,26}\text{Mg}$, ^{27}Al , $^{28,29,30}\text{Si}$, and ^{31}P .

3.3 Oxygen Burning

At Neon exhaustion the most abundant isotope is ^{16}O . At variance with ^{20}Ne , at the typical temperatures corresponding to neon exhaustion ($T \simeq 1.9 \times 10^9$ K), oxygen fusion is favored compared to its photodisintegration. Oxygen burning begins with the three ^{16}O fusion reactions, $^{16}\text{O}(^{16}\text{O}, p)^{31}\text{P}$, $^{16}\text{O}(^{16}\text{O}, \alpha)^{28}\text{Si}$ and $^{16}\text{O}(^{16}\text{O}, n)^{31}\text{S}(\beta^+)^{31}\text{P}$ (Fig. 5).

The branching ratios of these three reactions are $\sim 60\%$, $\sim 22\%$ and $\sim 18\%$ respectively. ^{31}P is converted into ^{28}Si , ^{30}Si , ^{32}S and ^{34}S via $^{31}\text{P}(p, \alpha)^{28}\text{Si}$, $^{31}\text{P}(\gamma, p)^{30}\text{Si}$, $^{31}\text{P}(\alpha, p)^{34}\text{S}$ and $^{31}\text{P}(p, \gamma)^{32}\text{S}$. Initially, one of the major products of neon burning, ^{24}Mg , is completely converted into ^{28}Si and ^{30}Si via the sequences $^{24}\text{Mg}(\alpha, p)^{27}\text{Al}$, followed by $^{27}\text{Al}(\alpha, p)^{30}\text{Si}$ and $^{27}\text{Al}(p, \gamma)^{28}\text{Si}$, and $^{24}\text{Mg}(\alpha, \gamma)^{28}\text{Si}$. Some ^{28}Si flows to ^{32}S and ^{29}Si via the reactions $^{28}\text{Si}(\alpha, \gamma)^{32}\text{S}$ and $^{28}\text{Si}(n, \gamma)^{29}\text{Si}$. Then ^{29}Si is almost completely converted into $^{32,33}\text{S}$ and ^{30}Si via (α, n) , (α, γ) and (n, γ) reactions. On the contrary, only a small amount of ^{32}S flows to ^{33}S , $^{35,37}\text{Cl}$ and $^{36,37}\text{Ar}$ through the sequences $^{32}\text{S}(n, \gamma)^{33}\text{S}$, $^{32}\text{S}(\alpha, p)^{35}\text{Cl}$, $^{32}\text{S}(\alpha, \gamma)^{36}\text{Ar}(n, \gamma)$

$^{37}\text{Ar}(e^-, \nu)^{37}\text{Cl}$. Some amount of ^{35}Cl , ^{38}Ar and ^{39}K is also produced via $^{34}\text{S}(\alpha, \gamma)^{37}\text{Ar}(p, \gamma)^{39}\text{K}$ and $^{34}\text{S}(p, \gamma)^{35}\text{Cl}$. Hence the main products of Oxygen burning are $^{28,30}\text{Si}$, ^{32}S , ^{34}S and ^{38}Ar . These species constitute $\sim 98\%$ of the final composition. Once again, also in oxygen burning lots of secondary channels contribute to the flow of the matter from O to the heavier isotopes. Hence the nucleosynthesis can be properly determined only by means of a nuclear network which includes lots of isotopes and reactions. Moreover the final composition after O burning (and in particular the relative abundance of the main products) can vary, even significantly, according to the temporal evolution of both temperature and density, that in turn depend on the mass of the star, and on whether the burning occurs in a convective core or in a convective shell. In oxygen burning the high temperatures favor the photodisintegration of the heavy nuclei (above iron), that were produced during carbon and neon burning by *s*-process nucleosynthesis, into Fe peak nuclei. The most efficient photodisintegration reactions are $^{57}\text{Fe}(\gamma, n)^{56}\text{Fe}$, $^{58}\text{Fe}(\gamma, n)^{57}\text{Fe}$, $^{59}\text{Co}(\gamma, p)^{58}\text{Fe}$, $^{64}\text{Ni}(\gamma, n)^{63}\text{Ni}$, $^{63}\text{Ni}(\gamma, n)^{62}\text{Ni}$, $^{63}\text{Cu}(\gamma, p)^{62}\text{Ni}$ and $^{64}\text{Cu}(\gamma, n)^{63}\text{Cu}$. During O burning some weak interactions become particularly efficient and may contribute significantly to the reduction of the electron fraction $Y_e = \sum_i X_i Z_i / A_i$ (for the first time after H burning where a substantial reduction of Y_e is due to the conversion of ^1H into ^4He). These are the electron captures $^{33}\text{S}(e^-, \nu)^{33}\text{P}$, $^{35}\text{Cl}(e^-, \nu)^{35}\text{S}$, $^{37}\text{Ar}(e^-, \nu)^{37}\text{Cl}$, $^{30}\text{P}(e^-, \nu)^{30}\text{Si}$ and the beta decay $^{31}\text{S}(\beta^+)^{31}\text{P}$. Once again, the efficiency of these reactions, and consequently the reduction of the electron fraction, significantly depends on whether the burning occurs in the center or in a shell. In general, the shell burning occurs at higher temperatures and lower densities compared to the central burning hence less electron captures occur there. Moreover the shell burning timescales are lower compared to the central burning. As a result a lower reduction of Y_e is found within the regions processed by shell oxygen burning.

3.4 The Intermezzo Between Oxygen and Silicon Burning

Near the end of oxygen burning isolated groups of nuclei coupled by strong and electromagnetic reactions nearly balanced by their reverses start to form. As the temperature increases, more isolated groups form and smaller groups merge into larger ones. At oxygen exhaustion the temperature is typically of the order of $T \simeq 2.5 \times 10^9$ K and one equilibrium cluster of isotopes, extending from $A = 24$ to $A = 44$, is formed. At $T \simeq 3.0 \times 10^9$ K another equilibrium cluster is formed and includes all the isotopes with $A \geq 46$. When the temperature is high enough ($T \simeq 3.5 \times 10^9$ K) the two equilibrium clusters eventually merge into one big equilibrium cluster which includes all the isotopes heavier than ^{24}Mg . This is the unavoidable consequence of the fact that the reaction rate of a reverse process is proportional to the reaction rate of the forward companion times $e^{-Q/kT}$, where Q is the Q-value of the forward process and T is the temperature of the plasma. When kT becomes larger than the Q , the inverse process begins to be efficient and eventually to fully balance its forward companion.

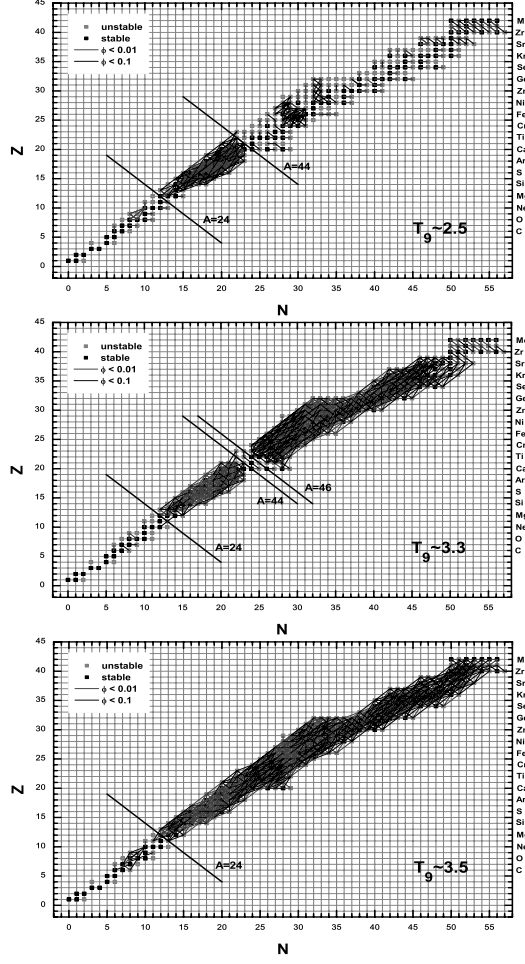


Fig. 6. Strong and electromagnetic reactions in the (N, Z) plane occurring at rates nearly balanced by their reverses ($\phi < 0.1$).

The sequence of events leading to the formation of one big equilibrium cluster is sketched in the three panels of Figure 6, each panel showing all the isotopes in the (N, Z) plane coupled by processes nearly at the equilibrium. Here we adopt as a measure of the degree of equilibrium reached by any couple of forward and reverse processes $i(k, l)j$ the ϕ parameter (as defined by [Chieffi et al. 1998](#)):

$$\phi(i, j) = \frac{|r_{ik} - r_{jl}|}{\max(r_{ik}, r_{jl})}. \quad (3.1)$$

This parameter tends to one if one of the two reactions dominates over its reverse companion, while it tends to zero as the two processes progressively approach the

equilibrium. At oxygen exhaustion one equilibrium cluster exists and includes all the isotopes with $24 \leq A \leq 44$ (upper panel of Fig. 6). This cluster contains more than 90% of the matter (the most abundant species at oxygen exhaustion are $^{28,30}\text{Si}$, ^{32}S , ^{34}S and ^{38}Ar). As the temperature rises above $T \simeq 3.0 \times 10^9$ K another cluster of isotopes with $A \geq 46$ forms (middle panel of Fig. 6). At this stage the matter begins to flow from the low- A to the high- A cluster via a series of reactions not yet in an equilibrium that bridge the two equilibrium clusters. The most efficient reactions that bridge the bottleneck between the two clusters are $^{44}\text{Sc}(p, \gamma)^{45}\text{Ti}(n, \gamma)^{46}\text{Ti}$, $^{44}\text{Sc}(n, \gamma)^{45}\text{Sc}(p, \gamma)^{46}\text{Ti}$, $^{45}\text{Sc}(n, \gamma)^{46}\text{Sc}$, $^{44}\text{Ca}(\alpha, n)^{47}\text{Ti}$. However, it must be noted that this sequence of reactions may change even significantly depending on the burning conditions. The general trend is that high temperature burning (occurring mainly in high mass stars) favors the passage of the matter through the proton rich side of the stability valley, while low temperature burning (typically in low-mass stars) activate non equilibrium reactions involving more neutron rich nuclei. When the temperature is high enough ($T \simeq 3.5 \times 10^9$ K) all the reactions linking the two equilibrium clusters reach an equilibrium with their reverses and the two groups eventually merge into one big equilibrium cluster (lower panel of Fig. 6). At this stage the most abundant species are still ^{28}Si ($\sim 60\%$), ^{30}Si and ^{34}S .

3.5 Silicon Burning

Silicon burning occurs in a completely different fashion compared to the previous nuclear burning stages. In fact, the presence of a big equilibrium cluster of isotopes with $A \geq 24$ limits the possibility of defining the leading processes driving the flow of the matter. Instead, ^{28}Si mainly burns by the sequence of photodisintegrations $^{28}\text{Si}(\gamma, \alpha)^{24}\text{Mg}$, $^{24}\text{Mg}(\gamma, \alpha)^{20}\text{Ne}$, $^{20}\text{Ne}(\gamma, \alpha)^{16}\text{O}$, $^{16}\text{O}(\gamma, \alpha)^{12}\text{C}$, $^{12}\text{C}(\gamma, 2\alpha)\alpha$ that are the most efficient reactions out of the equilibrium. The α particles released by this sequence add onto the big equilibrium group above ^{24}Mg and the composition of the equilibrium cluster readjusts on the new equilibrium abundance of the α particles and on the new abundance of ^{28}Si . Because of the fast rates of reactions induced by alpha particles and nucleons and of photodisintegrations of nuclei within the equilibrium cluster, the burning of ^{28}Si can be approximated by a succession quasi equilibrium states characterized by a ^{28}Si abundance and an equilibrium abundance of α particles. Each equilibrium state may be well described by a gas of nuclei following the Maxwell-Boltzmann distribution, at fixed temperature, fixed density and fixed ^{28}Si mass fraction, in which each nucleus (N, Z) is at an equilibrium with ^{28}Si under the exchange of protons, neutrons and alpha particles:

$$(N, Z) \rightleftharpoons ^{28}\text{Si} + \delta_\alpha \alpha + \delta_p p + \delta_n n \quad (3.2)$$

where δ_α , δ_p and δ_n specify the number of alpha, protons and neutrons in excess of the number in ^{28}Si . The number density of a species i in this gas of particles is given by:

$$n_i = e^{\mu_i/kT} \sum_r (2J_{i,r} + 1) e^{-\epsilon_{i,r}/kT} \left(\frac{2\pi m_i kT}{h^2} \right)^{3/2} \quad (3.3)$$

where the μ_i and m_i are the chemical potential and the mass of the species i respectively. The summation is over the ground state and excited states of the nucleus; $J_{i,r}$ and $\epsilon_{i,r}$ are the spin and the energy of the r 'th state above the ground state respectively. For simplicity we define:

$$\psi_i = e^{\mu_i/kT} \quad (3.4)$$

and

$$\omega_i = \sum_r (2J_{i,r} + 1) e^{-\epsilon_{i,r}/kT} \quad (3.5)$$

this last quantity being the partition function of the species i . Since the chemical equilibrium holds, the chemical potentials follow the relation:

$$\mu_{N,Z} = \mu_{^{28}\text{Si}} + \delta_\alpha \mu_\alpha + \delta_p \mu_p + \delta_n \mu_n + Q(N, Z) \quad (3.6)$$

where $Q(N, Z)$ is the energy required to decompose the nucleus (N, Z) into ^{28}Si , α 's and nucleons. As a consequence the following relation holds:

$$\psi_{N,Z} = \psi_{^{28}\text{Si}} \psi_\alpha^{\delta_\alpha} \psi_p^{\delta_p} \psi_n^{\delta_n} e^{Q(N,Z)/kT}. \quad (3.7)$$

By means of the relation 3.7 and by means of some algebra, Equation (3.3) becomes:

$$\begin{aligned} n(N, Z) &= \frac{\omega_{N,Z}}{\omega_{^{28}\text{Si}}} 2^{-\delta_p - \delta_n} \left(\frac{A(N, Z)}{A(^{28}\text{Si}) A(\alpha)^{\delta_\alpha}} \right) \\ &\times \left(\frac{m_H kT}{2\pi \hbar^2} \right)^{-3/2(\delta_\alpha + \delta_p + \delta_n)} e^{Q(N,Z)/kT} n_{^{28}\text{Si}} n_\alpha^{\delta_\alpha} n_p^{\delta_p} n_n^{\delta_n}. \end{aligned} \quad (3.8)$$

Where we have assumed $\omega_\alpha = 1$ and $\omega_p = \omega_n = 2$. Since the number density is related to the abundance by number Y by the following relation:

$$n = \frac{X}{A} \rho N_A = Y \rho N_A$$

Where X is the mass fraction, ρ is the density and N_A the Avogadro number, Equation (3.8) becomes:

$$Y(N, Z) = C(N, Z, \rho, T) Y(^{28}\text{Si}) Y_\alpha^{\delta_\alpha} Y_p^{\delta_p} Y_n^{\delta_n} \quad (3.9)$$

where the coefficient $C(N, Z, \rho, T)$ is given by:

$$\begin{aligned} C(N, Z, \rho, T) &= (\rho N_A)^{\delta_\alpha + \delta_p + \delta_n} \frac{\omega_{N,Z}}{\omega_{^{28}\text{Si}}} 2^{-\delta_p - \delta_n} \left(\frac{A(N, Z)}{A(^{28}\text{Si}) A(\alpha)^{\delta_\alpha}} \right) \\ &\times \left(\frac{m_H kT}{2\pi \hbar^2} \right)^{-3/2(\delta_\alpha + \delta_p + \delta_n)} e^{Q(N,Z)/kT}. \end{aligned} \quad (3.10)$$

Analogously the alpha particles are in equilibrium with protons and neutrons hence

$$Y_\alpha = C_\alpha Y_p^2 Y_n^2 \quad (3.11)$$

where

$$C_\alpha = (\rho N_A)^3 \frac{1}{16} 4^{3/2} \left(\frac{m_H k T}{2\pi \hbar^2} \right)^{-9/2} e^{Q_\alpha/kT} \quad (3.12)$$

(see Clifford & Tayler 1965; Bodansky *et al.* 1968). As the ^{28}Si gradually decreases, these equations have the general property of favoring the more bound iron peak nuclei corresponding to the actual neutron to proton ratio, *i.e.* the neutron excess. If the neutron excess is very small ($N \approx Z$), the main product of Si burning would be ^{56}Ni because it has the largest binding energy per nucleon among all isotopes having $N = Z$. However during Si burning weak interactions (mainly electron captures) are far from the equilibrium and drive the progressive increase of the neutronization (Limongi *et al.* 2000). As the neutron excess gradually increases, the more abundant isotope becomes ^{54}Fe or even ^{56}Fe . At the same time, the burning is not governed anymore only by (γ, α) photodisintegrations, but also by (p, α) and (n, α) reactions. Obviously, the preceding description was only a broad discussion of the sequence of events occurring during Si burning. A detailed computation of the nucleosynthesis during this nuclear burning requires the solution of the system of Equations (2.3) without any kind of equilibrium approximation.

For the typical burning conditions in the core of a massive star the chemical composition following Si burning mainly consists of ^{56}Fe and ^{52}Cr which account for more than $\sim 75\%$ of the total mass.

3.6 Nuclear Statistical Equilibrium

When the ^{28}Si mass fraction becomes very small, the chemical composition asymptotically approaches the nuclear statistical distribution where all the strong and electromagnetic reactions, including the (γ, α) photodisintegrations down to the α particles, are balanced by their reverses. In such Nuclear Statistical Equilibrium (NSE) all the nuclei (including ^{28}Si) are in equilibrium with exchange of protons and neutrons:

$$(N, Z) \rightleftharpoons Zp + Zn \quad (3.13)$$

hence Equation (3.9) becomes:

$$Y(N, Z) = B(N, Z, \rho, T) Y_p^Z Y_n^N \quad (3.14)$$

where

$$B(N, Z, \rho, T) = (\rho N_A)^{A-1} \frac{\omega_{N,Z}}{2^A} A(N, Z)^{3/2} \left(\frac{m_H k T}{2\pi \hbar^2} \right)^{-3/2(A-1)} e^{Q(N,Z)/kT}. \quad (3.15)$$

As a consequence once the NSE is achieved, the chemical composition can be expressed in terms of only three quantities, *i.e.*, temperature, density and neutron excess. As for Equations (3.9), also Equations (3.15) favor the nuclei corresponding to the actual neutron excess with the largest binding energy. However, when the temperature rises above $\sim 6 - 7 \times 10^9$ K, an increasing fraction of the matter is converted into lighter particles (mainly α particles). This causes a loss of energy

Table 2. Main products of the various nuclear burning stages in massive stars.

<i>Fuel</i>	<i>Main Products</i>	<i>Secondary Products</i>	<i>Elements Number</i>
¹ H	⁴ He	¹³ C, ¹⁴ N, ¹⁷ O	4, 7
⁴ He	¹² C, ¹⁶ O	¹⁸ O, ²² Ne, s – proc.	6, 8
¹² C	²⁰ Ne, ²³ Na ²⁴ Mg, ²⁷ Al	²⁵ Mg, s – proc.	10, 11, 12, 13
²⁰ Ne	¹⁶ O, ²⁴ Mg ²⁸ Si	^{25,26} Mg, ²⁷ Al ^{29,30} Si, ³¹ P	14, 15
¹⁶ O	^{28,30} Si, ^{32,34} S ³⁸ Ar	Cl, Ar K, Ca	14, 16, 17, 18 19, 20
²⁸ Si	⁵² Cr, ^{54,56} Fe	Ti, V, Cr Mn, Co, Ni	22, 23, 24, 25 26, 27, 28

corresponding to the difference in the binding energy between the initial and the final state. For example, by increasing the temperature from $T = 5 \times 10^9$ K to $T = 10 \times 10^9$ K, at fixed $\rho = 10^9$ g/cm³ and fixed $Y_e = 0.5$, the chemical composition changes from a matter dominated by ⁵⁶Ni (~ 0.9 in mass fraction) to a matter dominated by α particles (~ 0.9 in mass fraction) and this corresponds to an energy absorption of $\sim 2.4 \times 10^{15}$ erg/g. This property of the matter at high temperature is of great importance for the evolution of the iron core after core Si exhaustion as well as for the propagation of the shock wave generated by core bounce after core collapse within the iron core (see below).

The main products of each nuclear burning stages previously discussed are summarized in Table 2.

4 Presupernova Evolution

In the following sections we will describe the presupernova evolution of initially solar metallicity models in the mass range 11–120 M_{\odot} .

4.1 H and He Burning

The main evolutionary properties of massive stars during core H burning are reported in Table 3: initial mass in solar masses (Col. 1), maximum extension of the convective core in solar masses (Col. 2), total mass in solar mass at core H exhaustion (Col. 3), lifetime as O-type star in Myr (Col. 4), WNL lifetime in Myr (Col. 5) – the central H mass fraction at which the star enters the WNL stage is shown in parenthesis – and the He core mass in solar masses at core H exhaustion (Col. 6).

In massive stars core H burning occurs at temperatures in the range $3.5 \div 5.0 \times 10^7$ K (Table 1) and hence it is powered by the CNO cycle. Because of the strong sensitivity of this cycle on the temperature, the energy production is highly concentrated and this implies the presence of a convective core. The H convective core reaches its maximum extension at the very beginning of core H burning, then, as the burning proceeds, it recedes in mass and leaves a region of variable chemical composition that reflects the temporal variation of the central abundances. When the central H mass fraction drops below $\sim 10^{-7}$ the convective core vanishes and the H burning shifts in a shell. Central H burning lasts $\sim 20 \div 2 \times 10^6$ yr depending on the initial mass of the star in the range 11 – 120 M_{\odot} (Table 1).

Mass loss is quite efficient during this phase and scales directly with the mass (*i.e.* luminosity) of the star. Typically it ranges between 10^{-6} M_{\odot} /yr, for the 40 M_{\odot} , and 10^{-5} M_{\odot} /yr for the 120 M_{\odot} and induces in these stars a substantial reduction of the total mass (Table 3).

The location of core H burning massive stars in the HR diagram is shown in Figure 7. Stars with mass larger than ~ 13 M_{\odot} spent a fraction of their H burning lifetime as O-type stars (*i.e.* stars with effective temperature in the range $50\,000 < T_{\text{eff}} < 33\,000$) while stars below this limit do not enter this stage. This mass limit, however, depends on the details of the models.

The fraction of the core H burning lifetime spent as a O-type star (τ_H/τ_O) increases with the mass and ranges between ~ 0.15 for the ~ 14 M_{\odot} to ~ 0.80 for the ~ 120 M_{\odot} . This is the consequence of the occurrence that the higher is the mass the bluer is its MS location.

The H exhausted core (He core) that forms after core H burning scales directly with the initial mass of the star. Such a relation is not strongly affected by the mass loss, at least with the mass loss rates presently available in the literature. For example, for a 80 M_{\odot} model without mass loss, the He core at core H exhaustion is ~ 26 M_{\odot} while for the same model evolved with the mass loss rate provided by Vink *et al.* (2000), Vink *et al.* (2001) it reduces to ~ 22 M_{\odot} , *i.e.*, a reduction of only $\sim 5\%$, in spite of a reduction of $\sim 40\%$ of the total mass. On the contrary, the He core mass is strongly sensitive to the size of the H convective core that, in turn,

Table 3. Basic properties of the stellar models during core H burning.

M_{ini}	M_{CC}	M_{tot}	t_{O}	t_{WNL}	M_{He}
11	4.51	10.94			1.13
12	5.08	11.94			1.40
13	5.64	12.90			1.66
14	6.26	13.89	2.07		1.80
15	6.90	14.86	5.66		1.96
16	7.55	15.81	6.69		3.10
17	8.21	16.74	7.34		3.50
20	10.33	19.48	7.08		4.20
25	14.06	23.79	6.02		6.10
30	17.94	27.84	5.19		8.67
35	21.76	31.71	4.62		8.95
40	25.80	35.40	4.16		10.01
60	42.37	38.00	3.18		16.50
80	58.91	47.41	2.66		21.90
120	85.32	56.35	2.19	0.13(0.05)	37.30

strongly depends on the amount of overshooting included into the calculations. This also affects the location of the star in the HR diagram and hence has an indirect impact on the mass loss. On the other hand, the He core mass drives the following evolution of the star during core He burning, hence the convective core overshoot is still one of the major source of uncertainties in the computation of massive stars.

After core H exhaustion, the shell progressively advances in mass and settles at a mass coordinate corresponding to $\sim 60\%$ of the maximum extension of the previously H convective core. During this phase all the models move toward the red side of the HR diagram at roughly constant luminosity while the He core progressively contracts until the He burning reactions are activated. The following evolution of these stars is mainly driven by the competition between the efficiency of the mass loss in reducing the H-rich envelope during the red supergiant (RSG) phase and the He burning lifetime. In general, if the mass loss is strong enough to reduce substantially the H-rich envelope (uncovering the region of variable H) during the core He burning phase, the star moves quickly to the blue side of the HR

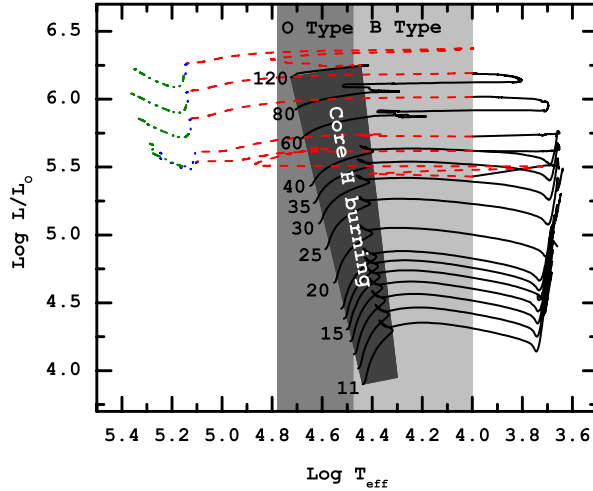


Fig. 7. Evolutionary paths of the stellar models in the HR diagram. The dark gray area corresponds to the region of core H burning models. The red dashed, blue dotted and green dotted dashed lines correspond to the WNL, WNE and WCO phases respectively. Also shown is the region of the O-type stars.

diagram, completes core He burning and explodes as blue supergiant (BSG). If, on the contrary, mass loss is not efficient enough to remove all the H-rich envelope before the core He exhaustion, it remains at the red side of the HR diagram and eventually explodes as RSG. The limiting mass between stars exploding as RSG and BSG is very sensitive on the mass loss rate. The following discussion is based on the mass loss rates provided by Vink *et al.* (2000), Vink *et al.* (2001).

Stars initially less massive than $\sim 30 M_{\odot}$ do not lose most of their H-rich envelope hence they complete their core He burning phase at the red side of the HR diagram and explode as RSG.

In stars with initial mass above this limit, on the contrary, the mass loss is efficient enough to significantly reduce the H-rich envelope. In particular, when the surface H mass fraction drops below ~ 0.4 the star quickly moves toward the blue, becomes a WNL Wolf-Rayet star (*i.e.*, a star having $H_{\text{sup}} < 0.4$ and $\text{Log} T_{\text{eff}} \geq 4.0$, according to the standard definition) and continues its core He burning phases as BSG. The fraction of core He burning lifetime spent by the star as RSG ($\tau_{\text{red}}/\tau_{\text{He}}$) depends on the central He mass fraction at which the star enters the WNL stage. In general the higher is the mass, the higher is the mass loss rate, the higher is the central He mass fraction at which the star enters the WNL stage and hence the lower is $\tau_{\text{red}}/\tau_{\text{He}}$ (Table 4).

As the stars approach their Hayashi track, a convective envelope appears and progressively penetrates in mass. When the convective zone reaches the mass coordinate corresponding to the maximum extension of the previously H convective

Table 4. Basic properties of the stellar models during core He burning (NL00; see text).

M_{ini}	M_{CC}	M_{tot}	M_{env}	$^{12}\text{C}_{\text{cen}}$	$t_{\text{red}}/\tau_{\text{He}}$	t_{WNL}	t_{WNE}	t_{WCO}
11	1.58	10.59	3.65	3.59(−1)	1.000			
12	1.84	11.52	4.13	3.61(−1)	1.000			
13	2.14	12.07	4.63	3.50(−1)	1.000			
14	2.44	12.83	5.14	3.41(−1)	1.000			
15	2.75	13.56	5.64	3.44(−1)	1.000			
16	3.06	14.25	6.14	3.47(−1)	1.000			
17	3.39	14.93	6.57	3.44(−1)	1.000			
20	4.60	16.47	8.07	3.21(−1)	1.000			
25	6.70	16.73	10.80	2.87(−1)	0.981			
30	8.79	13.07	13.50	2.63(−1)	0.872	0.04		
35	10.86	12.10	16.10	2.51(−1)	0.386	0.17	0.14	
40	12.56	12.57	18.80	2.47(−1)	0.167	0.11	0.20	0.02
60	19.49	17.16		2.18(−1)	0.022	0.06	0.13	0.15
80	27.77	22.74		1.87(−1)	0.000	0.04	0.08	0.18
120	40.20	30.97		1.56(−1)	0.000	0.05	0.05	0.20

core, the H burning processed material begins to be dredged up to the surface and eventually ejected into the interstellar medium through the stellar wind. Since stars above $\sim 60 M_{\odot}$ skip the RSG phase, a convective envelope is present only in models with initial mass below this limit (Table 4).

The main evolutionary properties of massive stars during core He burning are reported in Table 4: initial mass in solar masses (Col. 1), maximum extension of the convective core in solar masses (Col. 2), total mass in solar masses at core He exhaustion (Col. 3), mass coordinate in solar masses corresponding to the maximum depth of the convective envelope (Col. 4), central ^{12}C mass fraction at core He exhaustion (Col. 5), fraction of core He burning lifetime spent at the red side of the HR diagram (Col. 6), WNL, WNE and WCO lifetimes in Myr (Col. 7 to 9).

Core He burning occurs, as usual, in a convective core whose mass size either increases or remains fixed (at most). Such a behavior is typical of stars in which the He core mass remains roughly constant. In stars with initial mass greater than $M \sim 35 M_{\odot}$, on the contrary, mass loss is efficient enough ($10^{-5} - 10^{-4} M_{\odot}/\text{yr}$)

to uncover the He core first and to reduce progressively its mass later. Once this happens the star enters the WNE Wolf-Rayet stage (*i.e.* when $H_{\text{sup}} < 10^{-5}$ and $(C/N)_{\text{sup}} < 0.1$ according to the standard definition) and its following behavior during the remaining core He burning phase is driven by the actual size of the He core. In particular, as the He core progressively reduces in mass because of the mass loss, the star tends to behave as a star of lower mass (*i.e.*, star having the same actual He core) essentially by reducing its central temperature. Such an occurrence has the following effects: (1) the He convective core shrinks progressively in mass and leaves a region of variable chemical composition; (2) the core He burning lifetime increases; (3) the total luminosity progressively decreases, *i.e.*, the star in the HR diagram moves downward; (4) the ^{12}C mass fraction at core He exhaustion is larger than it would be without mass loss (see below); (5) the CO core at core He exhaustion is smaller than what would be without mass loss and resembles that of a star having a similar final He core mass (regardless on the initial mass of the star). Stars with initial mass greater than $M \sim 40 M_{\odot}$ experience a mass loss so strong that the total mass is decreased below the mass coordinate corresponding to the maximum extension of the He convective core. Once this occurs, the products of He burning start to be exposed to the surface and ejected into the interstellar medium through stellar wind and the star enters the WC Wolf-Rayet stage (*i.e.*, when $(C/N)_{\text{sup}} > 10$ according to the standard definition).

The relevance of the effects discussed so far, are very sensitive to the mass loss rate during the Wolf-Rayet stage. Figure 8 shows the CO core mass at core He exhaustion as a function of the initial mass for two different prescriptions of the mass loss during the WNE/WCO WR stages, *i.e.*, the one provided by Nugis & Lamers (2000, hereafter NL00) and the one provided by Langer (1989, hereafter LA89), the second one being higher by about 0.2-0.6 dex on average compared to the first one. From the figure it is clear that while in the case of the NL00 mass loss rate the CO core mass preserves a clear trend with the initial mass, in the case of the LA89 mass loss rate all the models show a very similar structure that resembles that of a lower mass models. It goes without saying that models with initial mass $M < 35 M_{\odot}$ do not differ between the two cases because they do not become WNE/WCO WR stars. The main properties of the LA89 models are reported in Table 5 (which shows the same quantities reported in Table 4). Another important difference between models computed with these two different prescriptions for the mass loss is the trend of the central ^{12}C mass fraction at core He exhaustion with the initial mass (Fig. 9). As for the CO core, also in this case, the LA89 models tend to behave like models having a similar final He core mass. Since the evolution of a massive star after core He burning is mainly driven by both the CO core mass and its chemical composition (mainly the C/O ratio), it is clear that the mass loss during the WR stage is fundamental in determining the evolutionary properties of these stars during the more advanced burning stages and also their final fate (see below).

Mass loss during both the RSG and the WR phases has a strong impact also on the total WR lifetime and on the specific lifetimes during the various WR stages. Let us recall few basic rules: (1) the higher the mass loss during the RSG phase

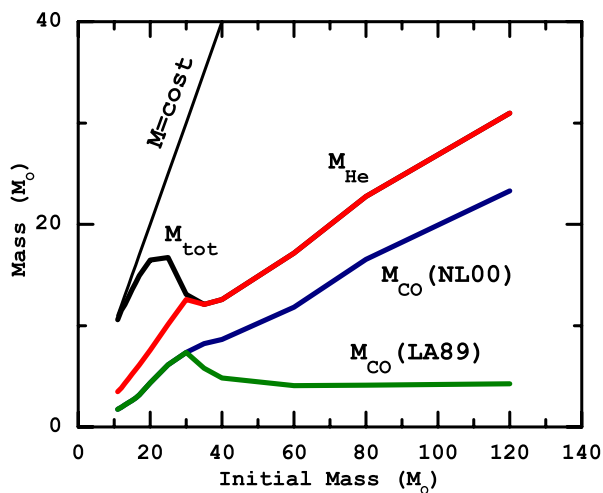


Fig. 8. Total mass, He core mass and CO mass at core He exhaustion as a function of the initial mass for two choices of the mass loss during the WR stage (see text).

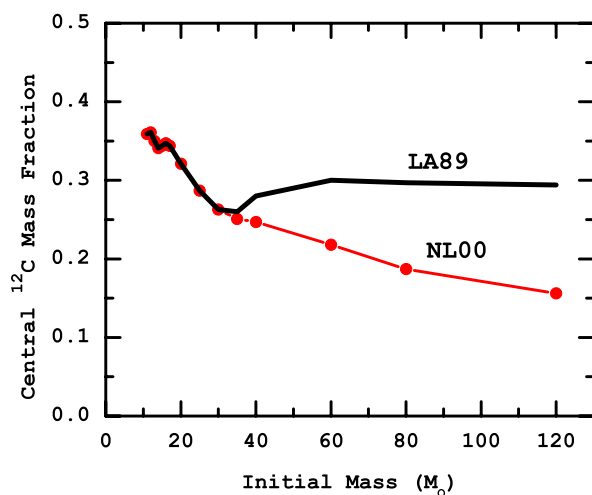


Fig. 9. Central ^{12}C mass fraction at core He exhaustion as a function of the initial mass for two choices of the mass loss during the WR stage (see text).

the earlier the stage (the higher the central He mass fraction) at which the star enters the WR phase; (2) the higher the amount of mass lost during the WR phase the lower the actual size of the He core, the longer the He burning lifetimes and hence the longer the WR lifetime (Tables 4,5).

Table 5. Basic properties of the stellar models during core He burning (LA89).

M_{ini}	M_{CC}	M_{tot}	M_{env}	$^{12}\text{C}_{\text{cen}}$	$t_{\text{red}}/\tau_{\text{He}}$	t_{WNL}	t_{WNE}	t_{WCO}
40	12.56	7.04	18.80	2.80(−1)	0.070	0.11	0.200	0.21
60	19.49	17.16		3.00(−1)	0.008	0.06	0.130	0.36
80	27.77	22.74		2.97(−1)	0.000	0.04	0.080	0.38
120	40.20	30.97		2.94(−1)	0.000	0.05	0.008	0.39

After the core He exhaustion, a CO core is formed and begins to contract in order to ignite the following nuclear fuel while the He burning shifts in a shell and induces the formation of a convective shell. In stars in which the He core remains constant in mass ($M < 35 M_{\odot}$) the He convective shell forms beyond the He discontinuity that marks the outer edge of the CO core, *i.e.*, in a region where the He profile is flat and equal to the one left by the H burning. Once the convective shell forms it advances in mass until it reaches its maximum extension. However, because of the short lifetimes of the advanced burning stages, only a small amount of He is burnt inside the shell before the final explosion of the star. In stars in which the He core is reduced by mass loss, on the contrary, the He convective shell forms in a region of variable chemical composition, *i.e.*, the region left by the receding He convective core. As a consequence the well known problem arises of whether the Schwarzschild or the Ledoux criterion must be used in order to determine if a convective regions actually forms. Since this is still an open question, one can explore the two limiting cases. In the first case, the shell is fully convective; it quickly advances in mass and reaches its maximum extension. In the second case, on the contrary, the shell is essentially radiative but, because of the short lifetimes of the advanced burning stages, it has no time to significantly advance in mass.

4.2 Advanced Burning Stages

The evolution of a massive star after core He exhaustion is mainly driven by the CO core mass and by its chemical composition, *i.e.*, mainly the $^{12}\text{C}/^{16}\text{O}$ ratio. ^{12}C and ^{16}O constitute the basic fuel for all the nuclear burning stages following core He burning up to the explosion and hence their relative abundance determine the behavior of the star during all the advanced burning stages. The $^{12}\text{C}/^{16}\text{O}$ ratio left by core He burning mainly depends on both the treatment of convection

during core He burning and the $^{12}\text{C}(\alpha, \gamma)^{16}\text{O}$ cross section (Imbriani *et al.* 2001). Unfortunately the physics of the convective motions is still poorly known and the determination of the total cross section of the $^{12}\text{C}(\alpha, \gamma)^{16}\text{O}$ reaction is still affected by large errors, hence these two ingredients constitute the two major uncertainties in the computation of the massive star models.

Once the He is exhausted inside the CO core, the He burning shifts in a shell while the CO core contracts in order to ignite the next fuel. The advanced evolutionary phases of massive stars are characterized by four major burnings, *i.e.*, carbon, neon, oxygen and silicon. In general each burning stage begins at the center and induces the formation of a convective core (Fig. 10). The convective core increases in mass, reaches a maximum and then disappears as the nuclear fuel is exhausted. The only exception to this general rule is core C burning that in the more massive stars ($M > 20 M_{\odot}$) occurs in a radiative environment due to the low ^{12}C mass fraction left by core He burning. Hence the limiting mass between stars burning C in a convective core and those in which C burning occurs in a radiative environment is sensitive to this quantity that, in turn, depends on both the treatment of convection and the $^{12}\text{C}(\alpha, \gamma)^{16}\text{O}$ cross section (see above).

Once the nuclear fuel is exhausted at the center, the burning shifts in a shell which in general is efficient enough to induce the formation of a convective zone above it (Fig. 10). Once the convective zone forms, the advancing of the shell stops and the burning proceeds within the convective shell. When the nuclear fuel is exhausted within all the convective zone, the burning shell quickly shifts outward in mass, where the main fuel is more abundant and eventually another convective zone forms. By the way, two successive convective shells may also partially overlap in mass and this may have some impact on the local nucleosynthesis. The details of this general behavior, *i.e.* number of convective zones formed in each burning stage and their overlap, depend on both the mass of the CO core (and hence the mass of the star) and its chemical composition.

In general, one to four carbon convective shells and two to three convective shell episodes for each of the neon, oxygen and silicon burnings occur. The number of C convective shells increases as the mass of the CO core decreases. For example in the $20 M_{\odot}$ model (CO core of $1.74 M_{\odot}$) three C convective shells form (Fig. 10) while in the $60 M_{\odot}$ model (CO core of $11.82 M_{\odot}$) only one convective zone forms (Fig. 11).

The complex interplay among the shell nuclear burnings and the timing of the convective zones determines in a direct way the distribution of the chemical composition and the mass-radius (M-R) relation of the star at the presupernova stage (the relevance of the M-R relation for the explosive nucleosynthesis is discussed in the next section). In general, the more efficient is the nuclear burning (*i.e.*, the higher is the ^{12}C mass fraction left by core He burning), the higher is the number of convective zones and the earlier is their formation (compare Fig. 10 and Fig. 11), the slower is the contraction of the CO core and the shallower is the final M-R relation. This means that the higher is the mass of the CO core, the more compact is the structure at the presupernova stage. In general the mass of the CO core scales directly with the mass, but if the mass loss is so strong to significantly

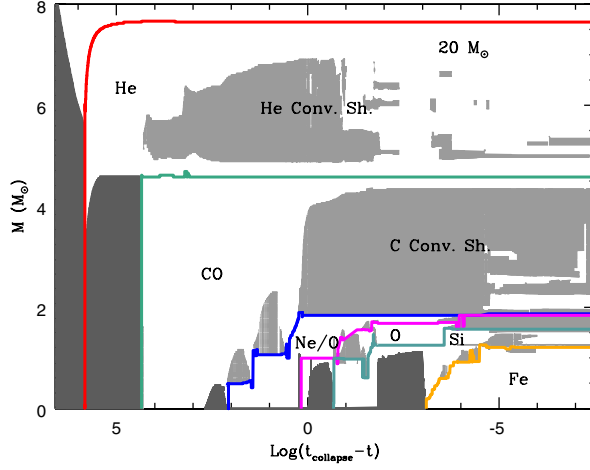


Fig. 10. Convective history in a $20 M_{\odot}$ model.

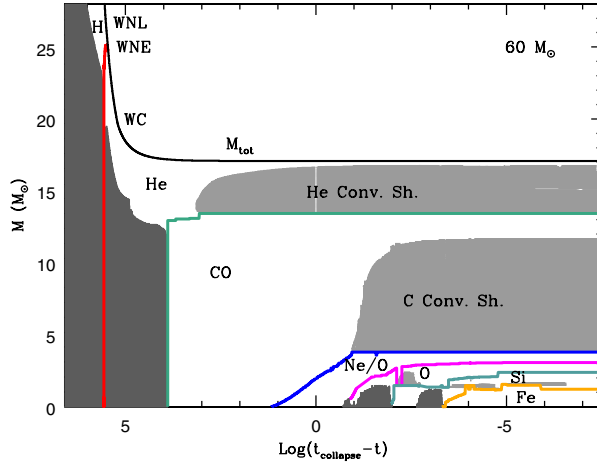


Fig. 11. Convective history in a $60 M_{\odot}$ model.

reduce the He core during core He burning, this scaling could not be preserved anymore (Fig. 8). The different scaling of the CO core mass with the initial mass directly reflects on the scaling between the initial mass and the final M-R relation. Figure 12 clearly shows that for the NL00 models the larger is the initial mass the more compact is the presupernova structure while, on the contrary, all the LA89 models have a very similar M-R relation at the presupernova stage. This is the consequence of the fact that the NL00 mass loss preserves a direct scaling between the initial mass and the CO core mass while, on the contrary, the LA89

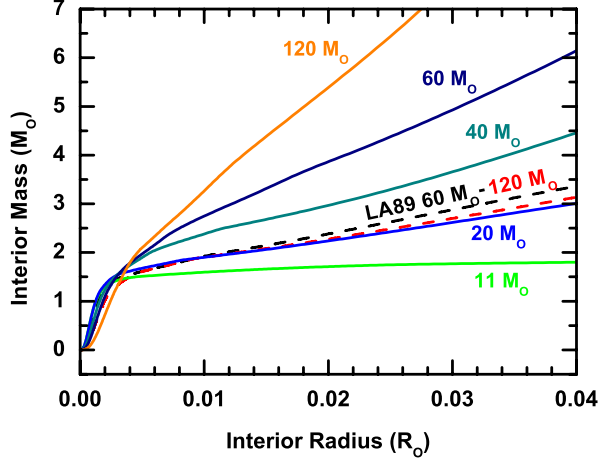


Fig. 12. M-R relation for a subset of massive star models at the presupernova stage. The solid lines refer to the NL00 models while the dashed lines correspond to the LA89 models respectively.

mass loss is so strong that all the LA89 models converge toward a very similar structure. By the way, all the LA89 models have a CO core mass similar to that of the $20 M_{\odot}$ computed with the NL00 mass loss. As a consequence all the LA89 models develop a final M-R relation close to that of the $20 M_{\odot}$ NL00 model.

The distribution of the most abundant chemical species at the presupernova stage is shown in Figure 13 for some selected models. The $25 M_{\odot}$ can be taken as representative of all the models in which the mass loss does not play a crucial role. On the contrary, the effect of mass loss is readily evident in the more massive stars. In general the presupernova star consists of an iron core of mass in the range between ~ 1.2 and $\sim 1.8 M_{\odot}$, depending on the initial mass of the star (Table 6, Col. 4), surrounded by active burning shells located at the base of zones loaded in the main products of silicon, oxygen, neon, carbon, helium and hydrogen burnings, *i.e.*, the classical “onion structure”. Thus, each zone keeps memory of the nucleosynthesis produced by the various central and/or shell burnings occurring either in a radiative environment or in a convective zone.

Summarizing, stars with initial solar metallicity behave as follows (at least in the present scenario). Stars with initial mass $M < 30 M_{\odot}$ retain a substantial fraction of their H-rich envelope hence will explode as RSG (Table 6, Col. 6) and will show the typical Type II-P SN display. On the contrary stars above this limit loose all their H-rich envelope hence will explode as BSG and will show either a Type Ib or a Type Ic SN display, depending on the composition of the envelope. In particular, in stars with initial mass $M < 40 M_{\odot}$ the envelope is dominated by He, hence they will likely explode as Type Ib SNe while in stars with initial mass $M \geq 40 M_{\odot}$ the envelope is dominated by ^{12}C and ^{16}O and hence they

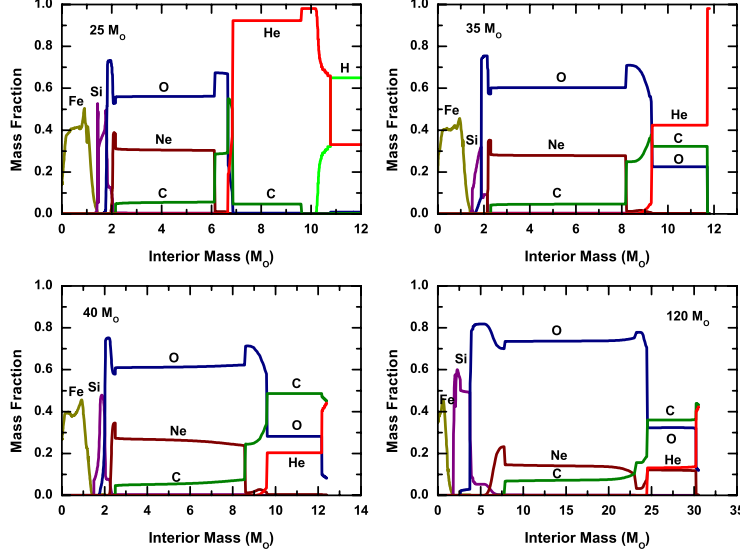


Fig. 13. Presupernova distribution of the most abundant chemical species for a selected number of massive star models.

will likely explode as Type Ic SNe. The basic properties of the stellar models at the presupernova stage are summarized in Table 6: initial mass in solar masses (Col. 1), maximum size of the He core in solar masses (Col. 2), maximum size of the CO core in solar masses (Col. 3), iron core mass in solar masses (Col. 4), total radius of the stars in cm (Col. 5), total lifetimes of WNL, WNE, WCO and WR stages in yrs (Col. 7 to 10).

5 Core Collapse and Bounce

Once the iron core is formed it contracts, as usual, in order to counterbalance the gravity. But, at variance with all the previous stages between two successive nuclear burnings, the following sequence of events will lead to the gravitational collapse of the iron core. First of all, it must be noted that at this stage the iron core is mainly supported by the partially degenerate electrons ($P_{\text{el}} \sim 10^{28}$ dyne/cm²) that dominate over the contribution given by both the radiation ($P_{\text{rad}} \sim 10^{26}$ dyne/cm²) and the ions ($P_{\text{ion}} \sim 10^{25}$ dyne/cm²) (see Fig. 15 in Limongi *et al.* 2000). The contribution of the Coulomb interactions are largely negligible at this stage. As the gravitational contraction proceeds, the density increases and this favors the electron captures onto the iron-group nuclei. This removes the major source of pressure against gravity, *i.e.*, the electrons. Moreover, as the temperature increases, following roughly the relation $T^3 \propto \rho$, the star enters a region in which the nuclear statistical equilibrium

Table 6. Basic properties of the stellar models at presupernova stage.

M _{ini}	M _{He}	M _{CO}	M _{Fe}	M _{Tot}	R _{fin}	t _{WNL} (tot)	t _{WNE} (tot)	t _{WCO} (tot)	t _{WR} (tot)
NL00									
11	3.47	1.74	1.33	10.56	2.27(13)				
12	3.84	1.95	1.23	11.49	2.54(13)				
13	4.30	2.17	1.47	12.01	2.82(13)				
14	4.76	2.41	1.45	12.77	3.17(13)				
15	5.23	2.62	1.38	13.49	3.36(13)				
16	5.69	2.87	1.42	14.16	3.63(13)				
17	6.13	3.16	1.43	14.83	3.89(13)				
20	7.57	4.35	1.46	16.31	5.23(13)				
25	10.13	6.13	1.42	16.35	6.81(13)				
30	12.58	7.36	1.47	12.92	7.93(11)	5.05(4)			5.05(4)
35	14.52	8.23	1.47	11.94	4.84(10)	1.16(5)	1.52(5)		2.68(5)
40	16.52	8.63	1.50	12.52	4.35(10)	1.10(5)	2.04(5)	2.64(4)	3.41(5)
60	24.62	11.82	1.65	17.08	4.19(10)	6.18(4)	1.28(5)	1.61(5)	3.51(5)
80	33.92	16.54	1.66	22.62	4.60(10)	4.43(4)	8.35(4)	1.91(5)	3.19(5)
120	47.53	23.31	1.81	30.83	6.04(10)	1.78(5)	5.35(4)	2.02(5)	4.33(5)
LA89									
40	16.52	4.83	1.50	6.88	3.08(10)	1.10(5)	5.43(4)	2.21(5)	3.86(5)
60	24.62	4.08	1.33	6.01	4.13(10)	6.18(4)	2.65(4)	3.78(5)	4.64(5)
80	33.92	4.13	1.46	6.10	4.00(10)	4.43(4)	1.53(4)	3.98(5)	4.57(5)
120	47.53	4.27	1.23	6.18	4.16(10)	1.78(5)	7.87(3)	4.08(5)	5.98(5)

distribution favors a large abundance of free α particles. The binding energy of this new configuration is lower than the previous one, *i.e.*, the one dominated by the iron peak nuclei, hence this process subtracts energy to the structure. These two instabilities favor the gravitational contraction of the iron core. When the electrons become relativistic, the adiabatic index becomes equal to 4/3 and the structure becomes unstable. A strong gravitational collapse begins. During the collapse the density increases progressively until, in the inner zones, it reaches the typical values of the nuclear matter, the equation of state suddenly stiffens, the collapse of the inner zones abruptly halts and a re-bounce is produced that launches a shock wave propagating outward in mass in the remaining portion of the iron core. In the past it was thought that this shock would be able to successfully trigger the explosion of the star (Baron *et al.* 1985), but now it does not seem the case.

Indeed, as the shock wave moves within the outer iron core it heats up the matter to very high temperatures and brings it to NSE distributions dominated by free neutrons and protons. Such a dissociation subtracts thermal (pressure producing) energy (see above) behind the shock, thereby weakening it. In addition to this energy loss, neutrino emission from behind the shock, *i.e.* in lower density regions ($\rho < 10^{12} \text{ g/cm}^3$), is very efficient and removes energy from the structure. Overall, the shock wave loses $\sim 10^{51}$ erg for each $0.1 M_{\odot}$ crossed. The result is that about 100 ms after the core bounce, the shock wave stalls at $\sim 200 - 300 \text{ Km}$ from the center. This constitutes the supernova problem, *i.e.*, realistic calculations show that for iron cores larger than $\sim 1.1 M_{\odot}$ the prompt shock cannot escape the outer edge of the core. Table 6 shows that the minimum iron core mass obtained in realistic evolutionary models of massive stars is $M_{\text{Fe}} \sim 1.2 M_{\odot}$. Then, a successful explosion requires an additional mechanism. This is the “delayed shock mechanism” initially discovered by Wilson (1985) and then fully developed by Behtze & Wilson (1985). In this mechanism, the stalled shock is re-energized by neutrino heating, *i.e.*, by the absorption of electron neutrinos and antineutrinos emerging from the radiating proto-neutron star by the free protons and neutrons behind it. This heating, however, depends sensitively on the neutrino luminosities, spectra and angle distribution in the region behind the shock, that in turn, depends on the neutrino transport and its coupling with the hydrodynamics equations governing the evolution of the collapsing core. Unfortunately, the most recent and detailed computations available at present show that either the shock still stalls or that the energy of the explosion is a factor of 3 to 10 lower than usually observed. Recent multidimensional calculations address the importance of neutrino transport, fluid instabilities, rotation and magnetic fields in generating core collapse supernova explosions, but the fundamental question as to whether or not these events are driven by neutrinos with the contribution of some or all of these other phenomena or by a combination of them is still unanswered. Work is underway by all the theoretical groups to better understand the problem and we may expect progresses in the next future.

6 Simulated Explosion and Explosive Nucleosynthesis

When the re-energized shock wave ultimately escapes the iron core it propagates through the mantle of the star and induces locally compression and heating. Since nuclear reactions are very temperature sensitive, this causes nucleosynthesis to occur within few seconds (the typical explosion timescales) that otherwise might have taken days or even years during the presupernova evolution. Due to the lack of a self consistent explosion model (see above), the explosive nucleosynthesis calculations occurring during these events are mainly based on induced explosions. The basic idea is to deposit a given amount of energy in a given mass zone of the presupernova model (typically at the outer edge of the iron core) and then follow the propagation of the shock wave that forms through the exploding mantle by means of a hydro code. The amount of energy injected into the presupernova model is tuned in order to have a given final kinetic energy at infinity (typically

of the order of 10^{51} erg = 1 foe). Historically, three different schemes have been adopted depending on the way in which the energy is injected into the progenitor star: (1) the kinetic bomb (the energy is deposited in the inner boundary in form of kinetic energy) (Limongi & Chieffi 2003; Chieffi & Limongi 2004 and their following papers); (2) the thermal bomb (the energy is deposited in form of thermal energy) (Thielemann *et al.* 1990; Thielemann *et al.* 1996 and their following works) and (3) the piston (the inner edge of the exploding mantle is moved like a piston following a given trajectory) (Woosley & Weaver 1995 and their following papers). Whichever is the technique adopted to inject the energy into the progenitor star (thermal bomb, kinetic bomb, piston or a mixture of these) and to follow the development of the shock wave, the result is that a fraction of the envelope is ejected into the interstellar medium with the required final kinetic energy, while some amount of matter (the innermost zones) falls back onto the compact remnant. The mass separation between remnant and ejecta is commonly defined as the *mass cut*.

Figure 14 shows the time history of the shock propagation during the explosion of a $25 M_{\odot}$ model in which the shock is induced by means of a kinetic bomb. The initial velocity is set to $v_0 = 1.555 \times 10^9$ cm/s and the final kinetic energy at the infinity is 1.144×10^{51} erg. Once the shock forms, it propagates outward in mass and induces locally compression and heating. Therefore, this triggers the explosive nucleosynthesis. Behind the shock front both the pressure and the density (and hence the temperature) are fairly constant in mass and progressively lower as the matter kicked by the shock wave expands and cools down. In $\simeq 4$ s the shock reaches the outer edge of the CO core; at this time the temperature in the shocked region decreased down to 10^9 K and the explosive nucleosynthesis ends. At $t \simeq 100$ s the inner zones of the mantle begin to fall back onto the compact remnant while the shock is still within the He core. The fall back lasts $\simeq 1 \times 10^5$ s though most of the mass that will ultimately return to the compact remnant actually falls back in just $\simeq 200$ s. The shock reaches the He/H interface at $t \simeq 370$ s after the formation of the shock and since this region corresponds to a very steep increase of ρr^3 , a reverse shock forms (Bethe 1990). This reverse shock propagates inward in mass and decelerates somewhat the expanding matter that it encounters in its way back: but it does not affect significantly the amount of fall back. The main outgoing shock reaches the surface of the star after $t \simeq 2 \times 10^5$ s, while the reverse shock escapes from the inner edge of the mantle after $t \simeq 6 \times 10^6$ s. The further evolution of the mantle is characterized by an homologous expansion ($v \propto r$) with velocity ranging between 1000 (inner zones) and 3000 km s⁻¹ (outer zones).

The basic properties of the explosive nucleosynthesis are mainly characterized by the temporal variation of both the temperature and the density of each zone of the exploding mantle during the explosion. Since the shock wave is almost adiabatic and radiation dominated, these properties can be derived, at first approximation, without the need of solving the whole hydrodynamic equations. In particular, since the pressure behind the shock is nearly constant (Fig. 14) and radiation dominated, the peak temperature at which each zone is heated up during

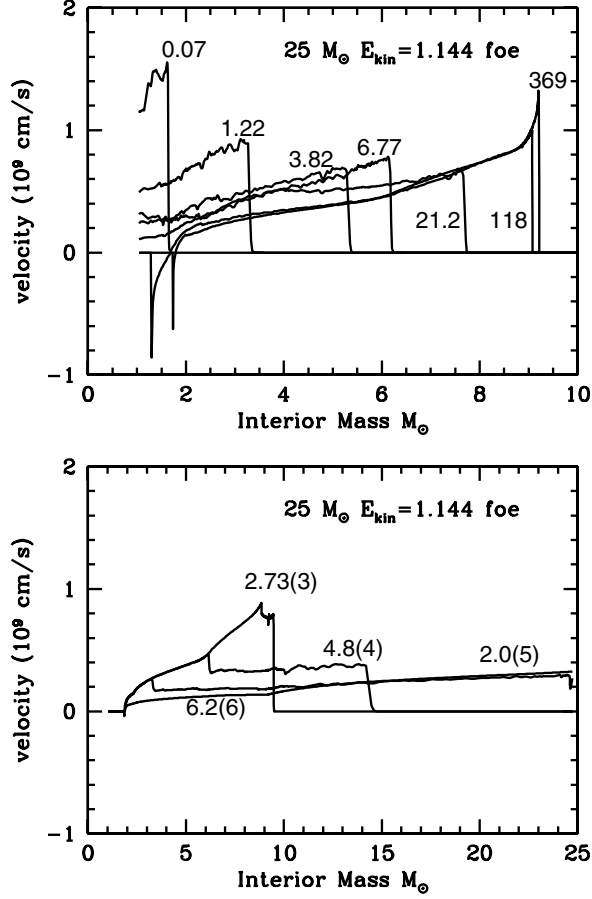


Fig. 14. Time history of the shock propagation in a $25 M_{\odot}$ model of initial solar composition. The shock is induced by means of a kinetic bomb with initial velocity $v_0 = 1.555 \times 10^9$ cm/s. The final kinetic energy at infinity is 1.144×10^{51} erg. Each line is labeled by the time in seconds at which it refers.

the explosion is given by:

$$E_{\text{expl}} = 4/3\pi R^3 a T_{\text{shock}}^4 \quad (6.1)$$

where a is the Stefan-Boltzmann constant, E_{expl} is the explosion energy, T_{shock} and R are the temperature of the shock and its spatial location. The shock density is derived by imposing the shock to be mildly strong, *i.e.*,

$$\rho_{\text{shock}} = 4\rho_{\text{preshock}}. \quad (6.2)$$

The temporal variation of the temperature and density in each zone is obtained by assuming the matter to expand adiabatically $T \propto \rho^{\gamma-1}$ at the escape velocity

$[v = (2GM/R)^{1/2}]$ and the density to decline following an exponential law, *i.e.*

$$\rho(t) = \rho_{\text{shock}} e^{-t/\tau} \quad (6.3)$$

where

$$\tau = \left(\frac{1}{\rho} \frac{\partial \rho}{\partial t} \right)^{-1} = \frac{R}{3v} = \frac{1}{\sqrt{24\pi G \rho}} = \frac{446}{\sqrt{\rho}}. \quad (6.4)$$

The main informations carried by Equation 6.1 (also confirmed by the hydrodynamic calculations) are the following: a) the peak temperature does not depend on the medium in which the shock wave propagates: this means that the progressive reduction of T_{shock} as the shock front propagates outward is a simple consequence of its adiabatic expansion (*i.e.*, a “geometrical effect”), independent on the properties (physical and chemical) of the presupernova model; b) the peak temperature corresponding to the various radii “R” has a very mild dependence on the explosion energy E_{expl} , since it scales as $E_{\text{expl}}^{1/4}$: this is a welcome property because it alleviates our ignorance regarding the real net energy of the shock escaping the iron core.

6.1 Explosive Burnings

The characteristic explosive burning temperatures can be estimated by the following relation:

$$\tau = \left| \frac{Y_i}{\dot{Y}_i} \right| \quad (6.5)$$

where i refers to the various fuels, namely, H, He, C, Ne, O and Si, and \dot{Y}_i is given by Equation (2.3) where only the major destruction reaction of each fuel is taken into account (see above). In general, the condition for explosive modification of the preexplosive chemical composition is that the burning lifetime corresponding to the shock temperature must be less than or comparable to the hydrodynamical timescale. If we take typical explosive burning timescales of the order of ~ 1 s, one finds that the temperature required in order to burn a substantial fraction of any given fuel must exceed $\simeq 4 \times 10^9$ K for Si, $\simeq 3.3 \times 10^9$ K for O, $\simeq 2.1 \times 10^9$ K for Ne and $\simeq 1.9 \times 10^9$ K for C. If the peak temperature is lower than $\simeq 1.9 \times 10^9$ K explosive modification is negligible and the matter is ejected without any further nuclear processing.

Zones heated up to temperatures in excess of $\simeq 4 \times 10^9$ K undergo explosive Si burning. For $T > 5 \times 10^9$ K all Coulomb barriers can be overcome, a full NSE is achieved (see above) and Si is completely converted into Fe peak nuclei. The relative abundance of these elements is a sensitive function of the local neutron excess. If $Y_e > 0.49$ the most abundant isotope produced is ^{56}Ni , which is the nucleus having the largest binding energy per nucleon for $N = Z$. However, in this regime, the chemical composition depends also on the expansion timescales. We have already mentioned that for temperatures $T > 6 \div 7 \times 10^9$ the NSE distribution is dominated by the α particles which may constitute even more than 90% of the

total mass. During the cooling phase which follows the passage of the shock front, the matter cannot (almost) instantaneously readjust on the NSE distribution of progressively lower temperatures since it exists another bottleneck which adds to the one already mentioned above, *i.e.*, the 3α reaction. This process is out of equilibrium and hence the build up of C occurs on timescales which may (and do) enter in competition with the cooling timescales whose main effect is, of course, that of freezing the chemical composition. In other words it exists a competition between the timescale of build up of the NSE population (which means essentially ^{56}Ni for a $Y_e > 0.49$), which is controlled by the efficiency of the 3α reactions, and the timescale of expansion which tends to freeze the chemical composition. This phenomenon, usually called “freeze out”, is well known and it has been firstly discussed by Truran *et al.* (1967) and recently by Thielemann *et al.* (1969). The normal “freeze out” occurs when most of the α particles may form C and hence the matter can (almost) instantaneously readjust on an equilibrium distribution which preferentially populates ^{56}Ni ; the α rich freeze out, on the contrary, occurs when the timescale of the expansion is much shorter than that of build up of C and in this case the final chemical composition is characterized by a large amount of free α particles and a low ^{56}Ni abundance. Also the regions that do not reach a temperature high enough to form preferentially α particles may experience a more or less faster “freeze out” but, in this case, the 3α process does not constitutes a bottleneck any more (simply because there are few α particles) and hence the matter can readjust (almost) instantaneously on the equilibrium distribution proper of the current value of the temperature until the “freeze out” temperature is reached. It goes without saying that a proper computation of the explosion of a massive star is of overwhelming importance in order to establish the timescales of expansion of the various layers (especially the ones closest to the “Fe” core) and hence, in turn, to obtain the kind of “freeze out” they will experience during the explosion. The chief products of complete explosive Si burning with normal “freeze out” are isotopes of Sc, Ti, Co, Ni and Zn (in addition to ^{56}Ni which is the most abundant one). The α -rich “freeze out” shifts the iron peak distribution to heavier nuclei transforming isotopes of Ni in isotopes of Zn. This also gives rise to a loading of ^{44}Ca as ^{44}Ti . In general, the relative proportions among these elements and, what it is more important, the relative abundances among the various isotopes is a function of ρ , T and Y_e .

For peak temperatures $4 \times 10^9 < T \text{ (K)} < 5 \times 10^9$ not all the processes can reach the full equilibrium with their reverses and in particular the first ones going out of the equilibrium are those linking isotopes having atomic masses $A = 44 - 46$ (Fig. 6 middle panel). Since the matter exposed to the explosion is essentially made of elements having $A \ll 44$, the main effect of this barrier is that the matter which quickly accumulates as ^{28}Si cannot redistribute freely upward but it will remain partially locked as ^{28}Si . Since the strength of this barrier increases as the temperature lowers, the abundance of ^{28}Si increases as the temperature decreases. In this temperature range the relative abundances of all the isotopes depend on T, ρ , Y_e and the amount of ^{28}Si itself. The main elements which form in this region

are Si, Ar and Ca. Partial leakage through the bottleneck above $A = 44$ produces V, Cr, Mn, Fe and ^{56}Ni .

Peak temperatures in the range $3.3 \times 10^9 < T \text{ (K)} < 4 \times 10^9$ lead to the formation of an equilibrium cluster extending in the range $24 < A < 44$ (Fig. 6 upper panel). The flux of the matter toward heavier nuclei is blocked at $A \simeq 44$. Within the low- A equilibrium cluster the abundance distribution is determined by T , ρ , Y_e and $\sum n_i$ (*i.e.* the sum by number of all the isotopes pertaining to the cluster). The weak interactions are negligible during the explosion hence the electron fraction remains constant and equal to the original pre-explosive one. Since these conditions are attained during the explosion in a region rich in oxygen, the most abundant isotopes produced by explosive oxygen burning are ^{28}Si , ^{32}S , ^{36}Ar and ^{40}Ca .

If the peak temperature remains confined within 3.3×10^9 and 1.9×10^9 K the direct and reverse strong processes are far from the equilibrium but both the temperature and the timescale of the expansion (cooling) of the matter are such that a significant amount of nuclear processing, mainly explosive Ne ($T > 2.1 \times 10^9$ K) and C burning ($T > 1.9 \times 10^9$ K) and/or a combination of them, may occur through efficient reaction rates: it is clear that in this case the final chemical composition will depend on the detailed preexplosive chemical composition, the reaction rates and the timescale of the expansion and not only on few parameters as T , ρ , Y_e and the like. Explosive Ne burning produces mainly ^{24}Mg , ^{27}Al , $^{29,30}\text{Si}$, ^{31}P and ^{37}Cl while explosive C burning mainly contributes to ^{20}Ne and ^{23}Na .

By combining the properties of the matter at high temperature and the basic properties of the explosion, we can define the volumes inside the star within which the various explosive burnings will occur. These volumes are independent on the structure of the presupernova star and, for an explosion energy of 10^{51} ergs, these correspond to the following radii (Fig. 15):

- a) 3700 Km – $T = 5 \times 10^9 \text{ K}$ – *NSE (complete Si burning)*
- b) 5000 Km – $T = 4 \times 10^9 \text{ K}$ – *2QSE clusters (incomplete Si burning)*
- c) 6400 Km – $T = 3.3 \times 10^9 \text{ K}$ – *1 QSE cluster (expl. O burning)*
- d) 11 750 Km – $T = 2.1 \times 10^9 \text{ K}$ – *nucl. burn. (expl. Ne burning)*
- e) 13 400 Km – $T = 1.9 \times 10^9 \text{ K}$ – *nucl. burn. (expl. C burning)*

The final chemical composition of a star layer exposed to the passage of the shock front will depend only on the volume in which it will be located at the moment of the passage of the shock. Let us notice here the pivotal role of a time delay between the collapse and the rejuvenation of the stalled shock in determining the final explosive yields: in fact, during this time delay (which may range between 0 up to more than 1 s.) the matter closer to the “Fe” core may significantly fall toward the center changing, even largely, the distribution of the mass (and, in turn, of the electron fraction Y_e) in the volumes defined above.

Complete Si burning $T > 5 \times 10^9 \text{ K}$ NSE	Incomplete Si burning $T > 4 \times 10^9 \text{ K}$ QSE 2 Clusters	Explosive O burning $T > 3.3 \times 10^9 \text{ K}$ QSE 1 Cluster	Explosive Ne burning $T > 2.1 \times 10^9 \text{ K}$	Explosive C burning $T > 1.9 \times 10^9 \text{ K}$	No Modification
Sc Ti Fe Co Ni	Cr V Mn	Si S Ar K Ca	Mg Al P Cl	Ne Na	
3700	5000	6400	11750	13400	
RADIUS (Km)					

Fig. 15. Schematic representation of the volumes inside the exploding star within which the various explosive burnings occur for an explosion energy of 10^{51} ergs.

6.2 Role of the Progenitor Star

The main property of the progenitor star that plays a crucial role in determining the final composition of the ejecta is the M-R relation at the presupernova stage (see above). In fact, the M-R relation fixes the total amount of mass which will be located in each of the volumes defined above (Fig. 15) and hence the total amount of mass which will be processed by each of the four different explosive burnings. As it was already discussed above, the M-R relation is the result of the superimposition of many successive (central and shell) hydrostatic burnings which obviously regulate the progressive contraction and heating of the core. Hence any uncertainty present in the computation of the various burning phase may reflect on the final M-R relation. Among the other factors let us mention the treatment of the convection and the cross section of the $^{12}\text{C}(\alpha, \gamma)^{16}\text{O}$ process as two of the major factors which may alter the quoted relation. Convection largely plays the major role in driving the evolution of a stellar model because it determines both the size of the convective regions and the efficiency of the mixing in these zones. The $^{12}\text{C}(\alpha, \gamma)^{16}\text{O}$ cross section contributes, together to the detailed treatment of the convection, to determine the $^{12}\text{C}/^{16}\text{O}$ ratio which is left by the central He burning: this ratio determines the amount of fuel which will be available for both the C and Ne burnings and hence both the possible formation of a convective core in these phases and the final location of their shells (see above). Also a possible time delay between the collapse and the rejuvenation of the shock would alter the M-R relation: the effect of the time delay is that of reducing the amount of matter which will fall within each of the various volumes. This effect is due to the occurrence that the speed of the various layers scales inversely with the distance from the center.

If the M-R relation essentially determines the total amount of matter subject to any given explosive burning, the Y_e profile determines its specific chemical composition (see above). Also the final Y_e profile will depend significantly on both the previous hydrostatic evolution of the star and on the possible time delay. In particular, once again, the final Y_e profile will be largely influenced by the efficiency of convection. To clarify this point let us remind that during the evolution of a star there are essentially four key points in which the neutronization of the matter changes significantly (*i.e.* Y_e reduces significantly). The first one is the H-burning phase in which two out of four protons become neutrons; the second one occurs when (during the He burning) the ^{14}N left by the CNO cycle is converted in ^{18}O via the sequence $^{14}\text{N}(\alpha, \gamma)^{18}\text{F}(\beta^+)^{18}\text{O}$; the third one occurs during the O-burning and it is due to a series of efficient weak processes (see Sect. 3.3) while the fourth one extends from the Si ignition onward and it is due to a very large number of weak processes which become efficient (see Chieffi *et al.* 1998; Limongi *et al.* 2000). The first two episodes of neutronization leave a flat Y_e profile within all the CO core because they do not depend on the physical conditions in which the burning occurs but only on the complete conversion of the H into He first and of the ^{14}N into ^{18}O later. By the way, the further conversion of ^{18}O in ^{22}Ne does not change Y_e . The two further episodes of neutronization, on the contrary, depend significantly on the mass (and unfortunately on the stellar model). The neutronization which occurs during the Oxygen burning obviously reduces Y_e only in the region where the burning has been efficient, *i.e.*, up to the external border of the last O-convective shell, and hence it will depend on the initial mass of the star (*i.e.* on its previous evolutionary history) and, in turn, on the specific stellar model. Also the last episode, which begins with the Si-ignition, modifies the neutronization up to the external border of the last Si convective shell. The interplay between these two burning shells will determine the final Y_e profile. Since the outer border of the Si shell marks the region highly neutronized which is usually assumed to remain locked in the remnant left by the explosion, two different possibilities exist: either the outer border of the last Si convective shell can extend beyond the outer border of the last O convective shell or not. In the first case the Y_e profile which will be exposed to the explosion will be essentially flat and hence it will not be altered by a possible infall. In the second case, on the contrary the Y_e profile will critically depend on the absolute location of the two borders; moreover in this case a possible infall may drastically change the Y_e which will be present in the volumes affected by the various kinds of burnings discussed above. Obviously the Y_e profile will lose importance in the more external regions where no equilibrium condition exists. In these outer regions the final yields largely depend on the chemical stratification of the presupernova model.

By combining the properties of the presupernova models to those of the explosion it is possible to identify which are the key parameters (and connected uncertainties) which influence the chemical composition of each of the zones described above (Fig. 16). In particular:

a) the total mass and the chemical composition of the matter confined between the mass cut and the radius corresponding to the peak temperature $T = 5 \times 10^9$ K

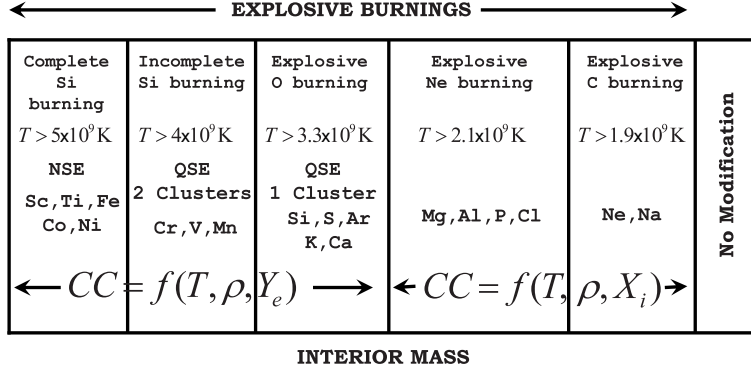


Fig. 16. Schematic representation of zones undergoing the various explosive burnings and the key parameters (and connected uncertainties) which influence the chemical composition of each one of these zones.

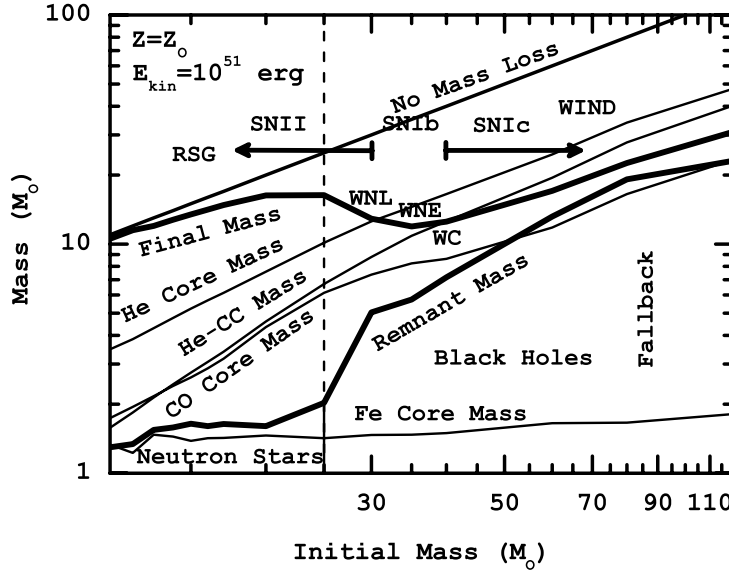


Fig. 17. Characteristic masses as a function of the initial mass for the NL00 models. The final kinetic energy at infinity is set to $E_{\text{kin}} = 1 \text{ foe}$.

(*i.e.*, the region in which full NSE is reached) is mainly determined by 1) the mass cut location itself, 2) the kind of freeze out, 3) the time delay, 4) the M-R relation and 5) the Y_e profile;

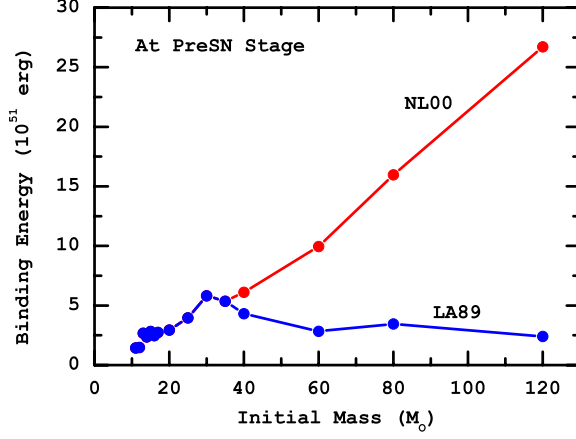


Fig. 18. Binding energy outside the iron core for NL00 and LA89 models.

b) the matter synthesized in the region heated up to temperatures in the range $4 \times 10^9 < T \text{ (K)} < 5 \times 10^9$ depends essentially on the same uncertainties which operate in the previous region;

c) the matter exposed to the third regime (*i.e.*, to the explosive Oxygen burning) is sensitive to: 1) the time delay (mildly), 2) the M-R relation and 3) the Y_e (actually it affects mainly the odd elements);

d) the mass undergoing explosive C and Ne explosive burning will depend on both the M-R relation and the detailed chemical composition preexisting the explosion.

e) the chemical composition of the zones located more externally than 13 400 Km from the center will totally depend on the presupernova evolution and not on the explosion.

A further parameter which must be mentioned and which alters the total amount of mass present in all of the four characteristic zones is the explosion energy since the radii corresponding to the four key temperatures scale as $E_{\text{expl}}^{0.5}$.

6.3 The Initial Mass-Remnant Mass Relation

As we have already mentioned above, even in the case of a successful shock, during the explosion some amount of matter may not reach the escape velocity and ultimately falls back onto the compact remnant. This happens if the shock energy is less than the binding energy of the mantle of the star.

The mass cut, *i.e.*, the mass separation between remnant and ejecta, strongly depends on the details of the explosive calculations, *i.e.*, the mass location and the way in which the energy is deposited, the inner and the outer boundary conditions, and so on, hence it constitutes the most uncertain and free parameter in the explosive nucleosynthesis calculations for core collapse supernovae. It strongly affects not only the chemical yields of all those isotopes that are produced in the

innermost zones of the exploding mantle, mainly ^{56}Ni and also all the iron peak elements (see above), but also the relation between the initial mass and the final remnant mass, *i.e.*, which is the mass limit or the mass interval between stars forming neutron stars and stars forming black holes after the explosion.

Figure 17 shows the the initial-final mass relation for the NL00 models, in the assumption that the ejecta have 1 foe of kinetic energy at infinity. This choice (*i.e.*, $E_{\text{kin}} = 1$ foe for all the models) implies that in stars with masses above 25-30 M_{\odot} all the CO core, or a great fraction of it, falls back onto the compact remnant. Such a behavior is the consequence of the fact that the higher is the mass of the star the steeper is the mass-radius relation (*i.e.* the more compact is the structure) (Fig. 12), the higher is the binding energy and hence the larger is, in general, the mass falling back onto the compact remnant. As a consequence these stars would not eject any product of the explosive burnings, as well as those of the C convective shell, and will leave, after the explosion, black holes with masses ranging between 3 and 11 M_{\odot} . In figure 17 the limiting masses that enter the various WR stages are also shown, *i.e.*, WNL (30 M_{\odot}), WNE (35 M_{\odot}) and WC (40 M_{\odot}), as well as the limiting mass (30 – 35 M_{\odot}) between stars exploding as Type II SNe and those exploding as Type Ib/c supernovae.

The behavior of the LA89 models is quite different because their binding energy is much smaller (Fig. 18) than their corresponding NL00 models due to the much smaller He core masses. In this case, the choice of a final kinetic energy of 1 foe allows, even in the more massive stars, the ejection of a substantial amount of the CO core, and hence heavy elements, leaving neutron stars as remnants (Fig. 19).

6.4 Chemical Yields

After the explosion all the matter above the mass cut is ejected into the interstellar medium. Since the ejecta contain all the products of both the hydrostatic and explosive nucleosynthesis, massive stars contribute significantly to the enrichment of the interstellar matter. The yields of the various elements, *i.e.*, the amount of mass (in solar masses) of each element present in the ejecta, are shown in Figures 20 and 21 as a function of the initial mass for the two set of models (LA89 and NL00).

The models with initial mass $M < 35 M_{\odot}$ do not differ between the two cases because they do not become WNE/WCO Wolf-Rayet stars. The yields of almost all the elements increase with the initial mass, for stars in this mass interval. In some cases, however, the dependence of the final yield on the initial mass is not monotonic. This is due to the fact that stars with similar (but not equal) mass may end up with even significantly different final structures and chemical abundances because of the complicated interplay between the various convective and burning shells occurring during the advanced burning stages (Limongi & Chieffi 2006).

For stars with initial mass $M \geq 35 M_{\odot}$, mass loss plays a crucial role in determining the final yields. Models with a lower mass loss rate (NL00) undergo a rather large fallback hence they do not eject all the products of complete and incomplete explosive Si burning (Sc, Ti, Cr, V, Mn and Fe) as well as elements

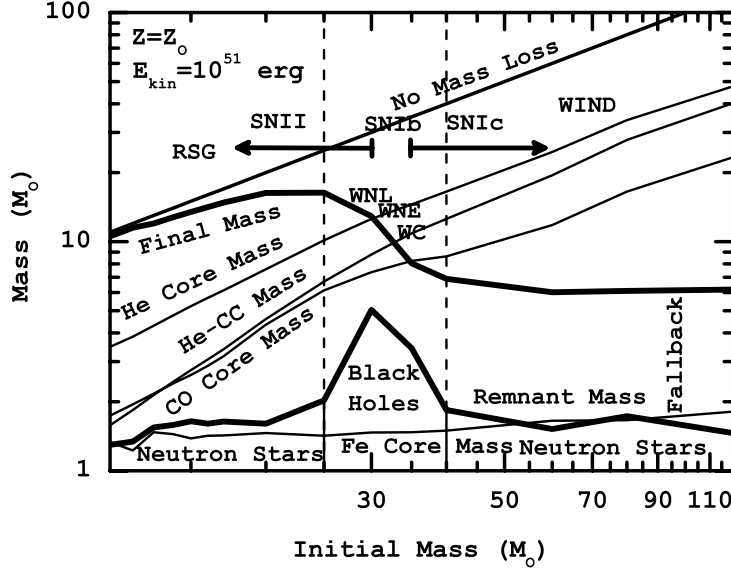


Fig. 19. Characteristic masses as a function of the initial mass for the LA89 models. The final kinetic energy at infinity is set to $E_{\text{kin}} = 1$ foe.

produced by explosive O burning (Si, S, Ar, K, and Ca). On the contrary, in the LA89 models the fallback is lower (Fig. 19) and a higher amount of all the elements produced in the innermost zones can be ejected into the interstellar medium in this case.

In order to determine the total contribution of a generation of massive stars to the global enrichment of the interstellar medium, as well as the relative contribution of the various masses, the yields shown in Figures 20 and 21 must be integrated over an initial mass function (IMF). The latest results obtained by Kroupa & Weidner (2003) and Kroupa (2004) seem to indicate that the IMF of stars with $M \geq 1 M_{\odot}$ is a power law with an exponent α as large as 2.8 and even larger if the binarity is taken into account. In spite of this, in order to maximize the role of massive stars we make use of the standard Salpeter IMF ($\alpha = 2.35$).

A useful quantity that puts in evidence the basic properties of the chemical yields provided by a generation of massive stars is the production factor (PF) of each element. The PF of any given isotope/element is defined as the ratio of each isotope's/element's mass fraction in the total ejecta divided by its corresponding initial mass fraction. Since in this case we are dealing with solar-metallicity models, the initial composition is the solar one. In general it is commonly accepted the idea that the ejecta of a generation of solar-metallicity massive stars should preserve the solar distribution of the various elements. In principle, there is no reason to require that because the solar system distribution is the result of the cumulative contribution of many generations of stars of very different metallicities. However,

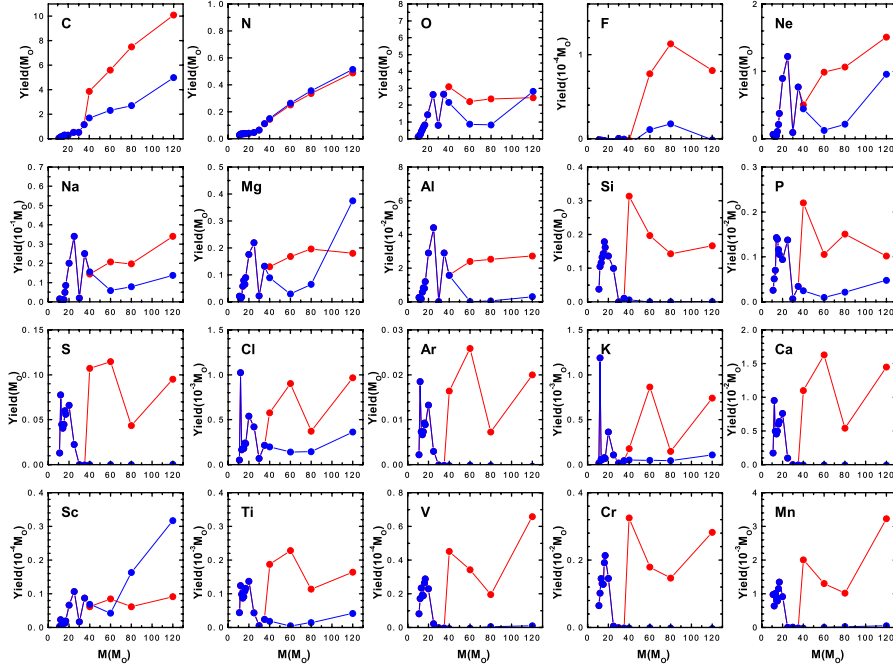


Fig. 20. Element yields as function of the initial mass for the NL00 (blue lines) and LA89 (red lines) models.

in the reasonable assumption that the average metallicity Z grows slowly and continuously with respect to the evolutionary timescales of the stars that contribute to the environment enrichment, the stars that mostly contribute to the abundances of the various nuclei at a given metallicity Z_0 are those whose initial Z is quite close to Z_0 . Since the assumption mentioned above is certainly well verified, at least for the massive stars, and very probably also for the intermediate-mass ones, it follows that most of the solar system distribution is the result (as a first approximation) of the ejecta of “quasi” solar-metallicity stars. This is the reason why it is desirable that a generation of solar-metallicity stars provides yields in roughly solar proportions or, in other words, that the PFs of the various nuclei remain roughly flat.

Figure 22 shows the PFs of all the elements provided by a generation of massive stars in the range $11\text{--}120 M_\odot$ averaged over a Salpeter IMF in the case of NL00 mass loss. The case of LA89 mass loss is not shown since it does not differ significantly with respect to the NL00 case. The first thing worth noting is that, on average, all the elements with atomic number $4 < Z < 38$ are overproduced by a factor ranging between ~ 2 and ~ 11 hence massive stars significantly contribute to the production of these elements (for some elements they even dominate). Since oxygen is produced predominantly by the core-collapse supernovae and is also the

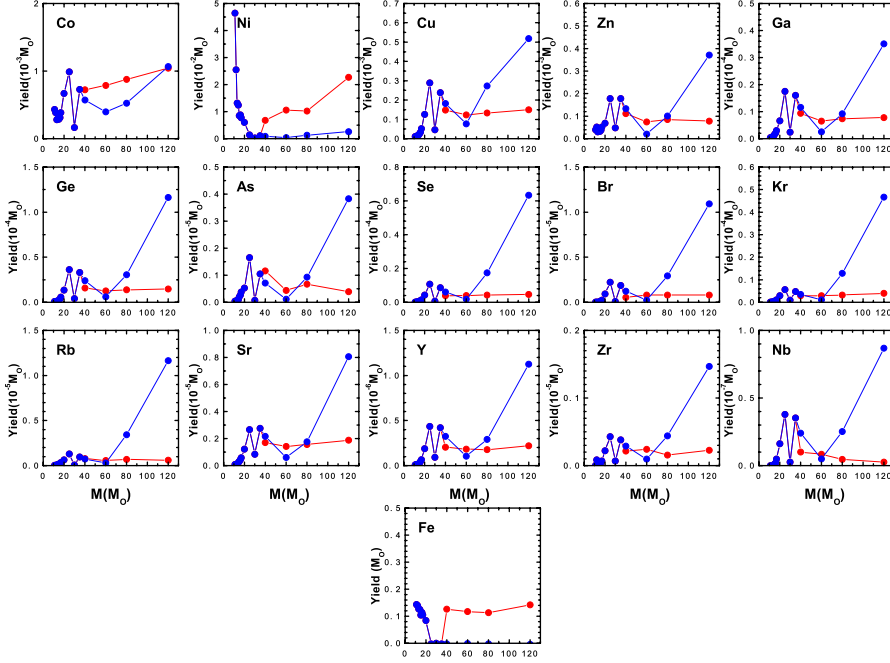


Fig. 21. Same as Figure 20.

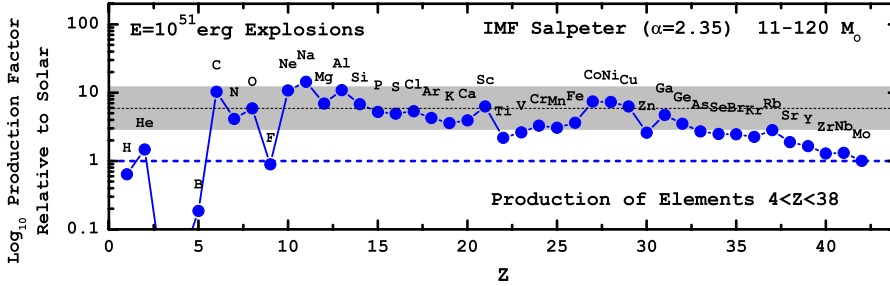


Fig. 22. Production factor of the elements from H to Mo for a generation of massive stars in the range 11–120 M_{\odot} averaged over a Salpeter IMF. The horizontal black dashed line refers to the production factor of Oxygen, PF(O), and the shaded area corresponds to a difference less than factor of 2 with respect to PF(O).

most abundant element produced by these stars, it is convenient to use its PF (horizontal black dashed line) as the one that better represents the overall increase of the average “metallicity” and to verify if the other nuclei follow or not its behavior. Arbitrarily we chose a factor of 2 (gray shaded area in Fig. 22) as a suitable warning threshold in the sense that we will assume that all the nuclei whose PF falls

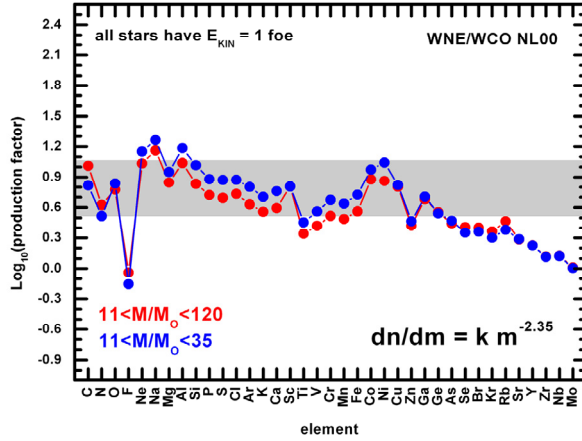


Fig. 23. Production factor of the elements from H to Mo for a generation of massive stars. The red and blue lines refer to an upper mass limit of 120 and 35 M_{\odot} respectively.

within a factor of 2 of the oxygen one are compatible with a flat distribution while those outside this compatibility range deserve a closer scrutiny and may potentially constitute a problem. Figure 22 shows that the majority of the elements from C to As have PFs compatible (in the sense mentioned above) with that of oxygen: the exceptions are F, Na, Ti, V, Zn, and the *s*-process elements heavier than As. F is largely underabundant (as expected) because our calculations do not include the neutrino induced reactions that contribute significantly to the synthesis of this element (Woosley & Weaver 1995). The overproduction of Na is not totally unexpected because this is a “secondary” element, *i.e.*, its production directly depends on the initial metallicity: the higher the initial metallicity, the larger its final production. Hence, its slight overproduction could simply indicate that the average metallicity to start with in order to get the solar system distribution should not be solar but slightly subsolar. It is worth reminding that the yield of this element strongly depends on the C abundance left over from the core He burning (Imbriani *et al.* 2001) hence the adoption of a different cross section for the $^{12}\text{C}(\alpha, \gamma)^{16}\text{O}$ process (still highly uncertain) may change, even significantly, the final yield of this element. Ti and V, as well as the other iron peak elements, are slightly underabundant compared to O. Such an occurrence, however, does not constitute a problem because Type Ia SNe contribute significantly to the production of these elements hence their inclusion would bring the PFs of the iron peak nuclei within the compatibility range. The PFs of the elements heavier than As are underproduced even largely (in the case of Sr, Y, Zr, Nb and Mo). Also in this case, this should not be a big problem since intermediate-mass stars contribute significantly to the production of these elements.

In order to stress the role played by stars more massive than 35 M_{\odot} , *i.e.*, stars that become WNE/WCO Wolf-Rayet, we show in Figure 23 a comparison between

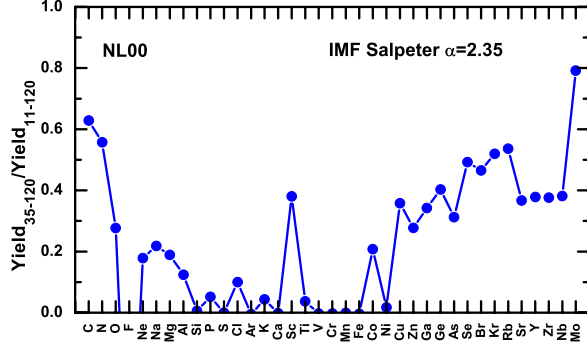


Fig. 24. Contribution of the stars with initial mass $M \geq 35 M_{\odot}$ to the total yields when the NL00 mass loss rate is adopted for the models that enter the WNE/WCO phases.

PFs obtained by integrating the IMF with two different upper mass limits, *i.e.*, $120 M_{\odot}$ (red line) and $35 M_{\odot}$ (blue line) respectively. Obviously the two sets of PFs have a different normalization since each one is normalized to $1 M_{\odot}$ of gas converted in mass following the chosen IMF. The close similarity between the two PFs indicates that stars more massive than $35 M_{\odot}$ do not produce any specific signature on the integrated IMF. However, this does not mean that they do not contribute to the production (in solar masses) of none of the elements shown in the Figure. Figure 24 shows the contribution of the more massive stars ($M \geq 35 M_{\odot}$) to the total yield of each element in the case of NL00. A look to Figure 24 shows that these stars produce $\sim 60\%$ of the total C and N, $\sim 40\%$ of the total Sc and *s*-process elements, while they do not contribute at all to the production of the intermediate-mass and iron peak elements. The large contribution to the global synthesis of C, N is due to the strong mass loss experienced by these stars that allows the ejection of these nuclei before their destruction by the successive burnings. Also the elements mainly produced by the He burning (the weak *s*-component plus Sc) are significantly produced by these stars because a large fraction of the matter processed by the He convective core is ejected anyway in the interstellar medium, in spite of the large remnant mass. On the contrary, the very low contribution of these stars to the production of the intermediate-mass and iron peak elements is the direct consequence of the large amount of fall back experienced by the models.

The adoption of the LA89 mass loss rate for stars that enter the WNE/WCO stages ($M \geq 35 M_{\odot}$) does not modify significantly the results shown in Figure 23. However, the relative contribution of these stars to the total yields (Fig. 25) changes significantly with respect to the one shown in Figure 24. In particular, with the adoption of the LA89 mass loss rate, stars with $M \geq 35 M_{\odot}$ contribute for $\sim 30\%$ to the production of most of the elements and for $\sim 80\%$, $\sim 55\%$ and more than $\sim 100\%$ (this means that stars with $M < 35 M_{\odot}$ destroy this element) to the production of C, N and F, respectively. The non negligible contribution to the majority of the elements is due to the rather small amount of fall back that

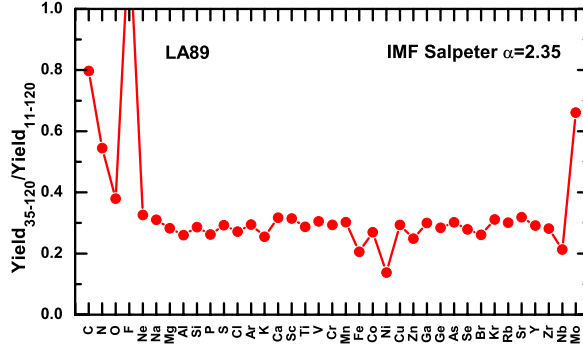


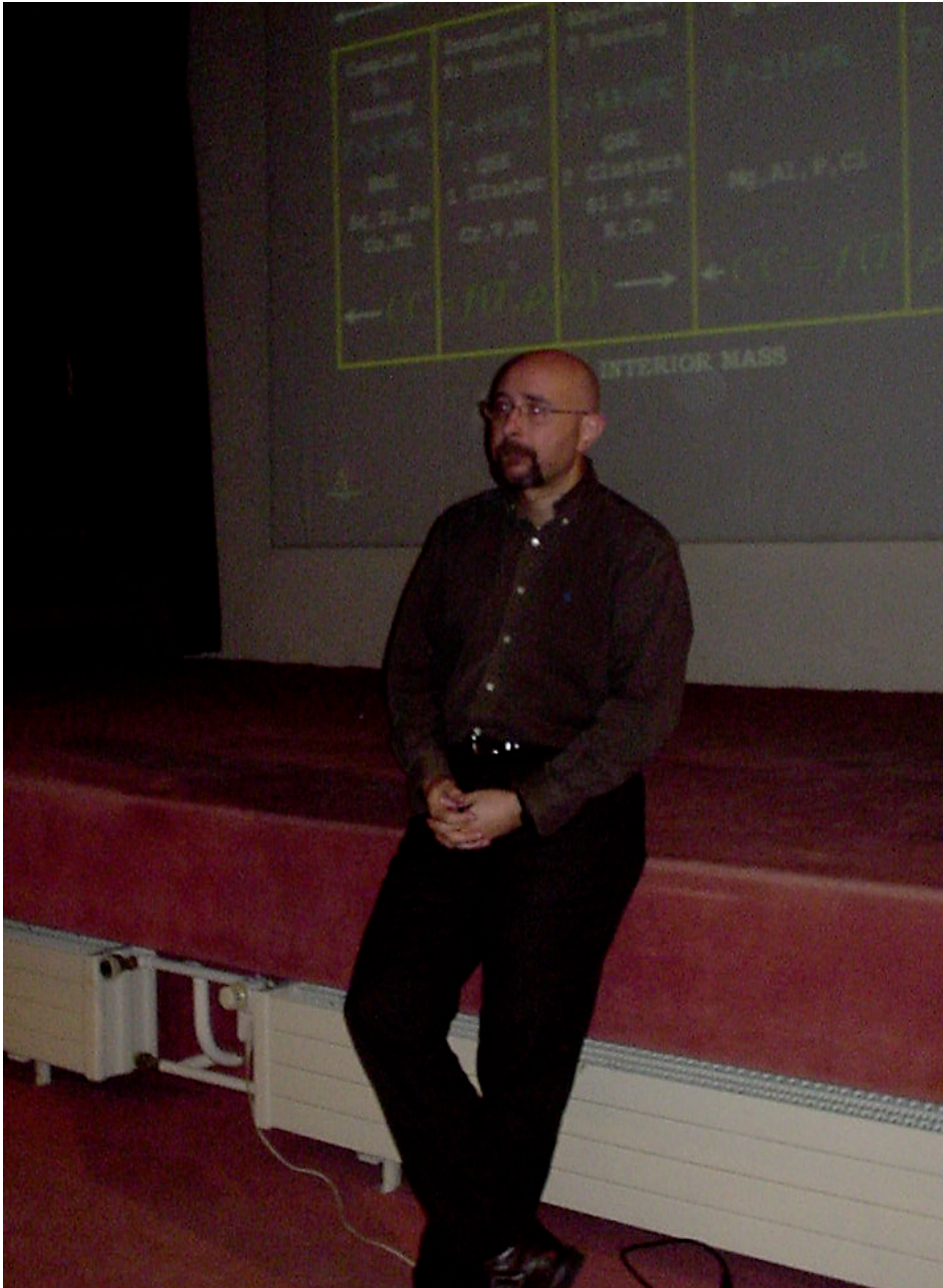
Fig. 25. Contribution of the stars with initial mass $M \geq 35 M_{\odot}$ to the total yields when the LA89 mass loss rate is adopted for the models that enter the WNE/WCO phases.

allows the ejection of a substantial amount of elements produced in the innermost zones of the exploding mantle. The large contribution to C, N and F is due to the very efficient mass loss that preserves them from further destruction. It is worth mentioning, however, that the contribution of the very massive stars to the chemical enrichment of the Galaxy, shown in Figures 24 and 25, is very probably an upper limit since the IMF of these stars should be much steeper than a Salpeter one.

References

- Abbott, D.C., 1982, ApJ, 263, 723
 Baron, E., Cooperstein, J., & Kahana, S., 1985, Phys. Rev. Lett., 55, 126
 Bethe, H., & Wilson, J.R., 1985, ApJ, 295, 14
 Bethe, H.A., 1990, Reviews Mod. Phys., 62, 801
 Bloom, J.S., *et al.*, 2002, ApJ, 572, L45
 Bodansky, D., Clayton, D.D., & Fowler, W.A., 1968, ApJS, 16, 299
 Bromm, V., Kudritzki, R.P., & Loeb, A., 2001, ApJ, 552, 464
 Bromm, V., Yoshida, N., & Hernquist, L., 2003, ApJ, 596, L135
 Burbidge, E.M., Burbidge, G.R., Fowler, W.A., & Hoyle, F., 1957, Rev. Mod. Phys., 29, 547
 Clifford, F.E., & Tayler, R.J., 1965, Mem. R.A.S., 69, 21
 Chieffi, A., Limongi, M. & Straniero, O., 1998, ApJ, 502, 737
 Chieffi, A., & Limongi, M., 2004, ApJ, 608, 405
 Fowler, W.A., Caughlan, G.R., & Zimmerman, B.A., 1975, ARA&A, 13, 69
 Imbriani, G., Straniero, O., Terrasi, F., Limongi, M., & Chieffi, A., 2001, Nuc. Phys. A, 688, 249
 Kroupa, P., 2004, New Astron. Rev., 48, 47
 Kroupa, P., & Weidner, C., 2003, ApJ, 598, 1076

- Langer, N., 1989, A&A, 220, 135 (LA89)
- Limongi, M., Straniero, O., & Chieffi, A., 2000, ApJS, 129, 625
- Limongi, M., & Chieffi, A., 2003, ApJ, 592, 404
- Limongi, M., & Chieffi, A., 2006, ApJ, 647, 483
- Maeder, A., & Conti, P.S., 1994, ARA&A, 32, 227
- Massey P., 2003, ARA&A, 41, 15
- Mori, M., Ferrara, A., & Madau, P., 2002, ApJ, 571, 40
- Nakamura, T., Umeda, H., Iwamoto, K., *et al.*, 2001, ApJ, 555, 880
- Nomoto, K., & Hashimoto, M.-A., 1988, Phys. Rep., 163, 13
- Nugis, T., & Lamers, H.J.G.L.M., 2000, A&A, 360, 227 (NL00)
- Price, P.A., *et al.* 2002, ApJ, 572, L51
- Rauscher, T., Heger, A., Hoffman, R.D., & Woosley, S.E., 2002, ApJ, 576, 323
- Thielemann, F.-K., & Arnett, W.D., 1985, ApJ, 295, 604
- Thielemann, F.-K., Hashimoto, M.-A., & Nomoto, K., 1990, ApJ, 349, 222
- Thielemann, F.-K., Nomoto, K., & Hashimoto, M.-A., 1996, ApJ, 460, 408
- Thielemann, F.-K., Rauscher, T., Freiburghaus, C., *et al.*, 1999, in Nuclei and Particles Physics, eds. J. Hirsh and D. Page (Cambridge University Press)
- Truran, J.W., Arnett, W.D., & Cameron, A.G.W., 1967, Canadian J. Phys., 45, 2315
- Tumlinson, J., & Shull, J.M., 2000, ApJ, 528, L65
- Umeda, H., & Nomoto, K., 2002, ApJ, 565, 385
- Umeda, H., & Nomoto, K., 2005, ApJ, 619, 427
- Vink, J.S., de Koter, A., & Lamers, H.J.G.L.M., 2000, A&A, 362, 295
- Vink, J.S., de Koter, A., & Lamers, H.J.G.L.M., 2001, A&A, 369, 574
- Wada, K., & Venkatesan, A., 2003, ApJ, 591, 38
- Weaver, T.A., Zimmerman, G.B., & Woosley, S.E., 1978, ApJ, 225, 1021
- Weaver, T.A., Woosley, S.E., & Fuller, G.M., 1985, in Numerical Astrophysics, ed. J.M., Centrella, J.M., LeBlanc & R.L., Bowers (Boston: Jones & Bartlett), 374
- Wilson, J.R., 1985, in Numerical Astrophysics, ed. J.M., Centrella, J.M., LeBlanc & R.L., Bowers (Jones and Bartlett Publishers, Inc., Boston, 1985), 442
- Woosley, S.E., & Weaver, T.A., 1982, in Essays in Nuclear Astrophysics, ed. C.A., Barnes, D.D., Clayton, & D.N., Schramm (Cambridge: Cambridge Univ. Press), 377
- Woosley, S.E., 1993, ApJ, 405, 273
- Woosley, S.E., & Weaver, T.A., 1995, ApJS, 101, 181
- Yoshida, N., Bromm, V., & Hernquist, L., 2004, ApJ, 605, 579



Copyright of EAS Publications Series is the property of EDP Sciences and its content may not be copied or emailed to multiple sites or posted to a listserv without the copyright holder's express written permission. However, users may print, download, or email articles for individual use.